

# Study on Autonomous Power Management for Wireless Telecommunication

Jihun Koo

Smart IT department  
Osan University  
Osan-si, Republic of Korea  
Jihun.koo@osan.ac.kr Jihun Koo

Hayoung Yoon

Digital Contents Design department  
Osan University  
Osan-si, Republic of Korea  
yoon@osan.ac.kr

**Abstract**—This paper presents an effective autonomous power management (APM) that includes hardware architecture, power management policies, and control algorithms. Architecture designs have been proposed to integrate modems and application processors for wireless communication. APM is designed to reduce power consumption in non-time-consuming tasks such as wireless communications. Perform electronic system-level simulations to evaluate the proposed architecture to determine device performance and power consumption. Simulation results show that the proposed architecture can meet the performance and energy consumption requirements of the proposed application processor.

**Keywords**— *dynamic power management (DPM), dynamic voltage/frequency scaling (DVFS), system-on-chip (SoC), Wireless communication*

## I. INTRODUCTION

In general, smartphones and tablet PCs comprise two representative components: application processor (AP) and modem processor (MP). The former is used for supporting multimedia applications including games, music, movies, camera, and web surfing. Therefore, for high performance and diverse functions, the APs have become more complex and larger [1], [2]. The latter is designed for voice and data personal telecommunication with the base stations. The MPs have been implemented with full-range communication protocols such as code division multiple access (CDMA), global system for mobile communication (GSM), and wideband CDMA (WCDMA), and long-term evolution (LTE).

As shown in Fig. 1 (a), the conventional smartphones comprise a dedicated MP and a dedicated AP with an independent memory. Each main memory is a type of low-power double data rate (LPDDR) synchronous dynamic random-access memory (SDRAM). However, for removing the memory on the side of the MP and share the memory in the AP, diverse inter-chip connectivity technologies have been introduced, such as USB HSIC, MIPI LLI, and C2C [3], as shown in Fig. 1 (b). When an end user does not use any application program, that is, when a dedicated AP is not used, the AP transits into the power-saving mode. However, at that time, a dedicated MP is periodically operated to communicate with the base station.

As an emerging trend in the telecommunication industry,

the duumvirate in the smartphone has transformed into a union. In other words, a new SoC has been merged with an AP and an MP, as shown in Fig. 1 (c). We call this SoC an integrated modem/application processor (IMAP), which can reduce the costs, size, time, power consumption, and bill of the materials used. In addition, as a significant challenge for the IMAP, we have attempted to integrate a shared-memory architecture between the MP and the AP, as shown in Fig. 1 (d). Actually, the size and power consumption of the DDR are greater in the IMAP. For sharing the high-capacity main memory in the AP with the MP block, the MP block needs to use the high-performance system bus for accessing the memory in the AP. Although the system bus is an energy consuming block, which is designed for high performance and high speed, the common blocks cannot enter into the power saving mode because of the use of the MP block in the case of the shared-memory structure.

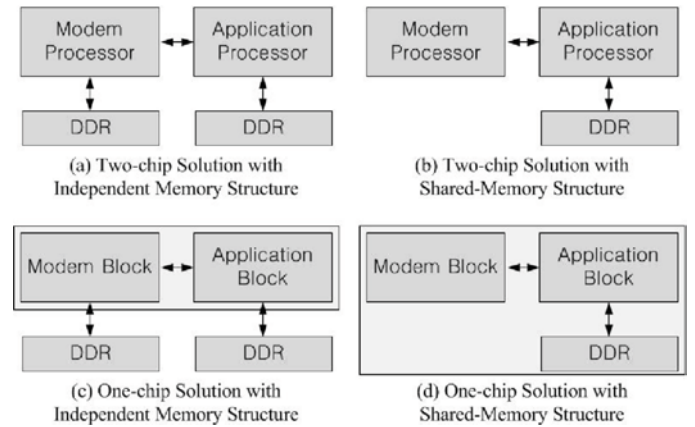


**Fig. 1** Classification of architectures for smartphones based on relations between modem processor, application processor, and main memory

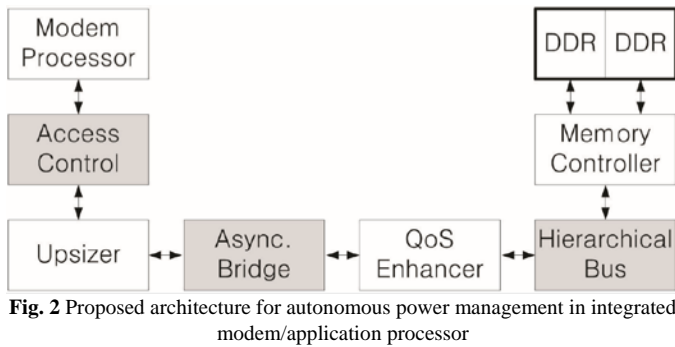
## II. ARCHITECTURE FOR AUTONOMOUS POWER MANAGEMENT

Most of the recently designed SoCs for mobile devices have adopted the diverse power management scheme: DVFS[5], DPM, clock control, and dynamic self-refresh for the memory. However, for the architecture of the shared-memory of the IMAP, it is necessary to design a novel algorithm for satisfying the time constraints for telecommunication. For reducing the

This work was supported by the Technology development Program(S2599981) funded by the Ministry of SMEs and Startups(MSS, Korea).

energy consumption of the shared-memory architecture, the entire architecture, not the individual components, should be considered [31].

In this subsection, an APM is addressed to design an architecture for reducing the power consumption with sensitive response speed. The APM is easily implemented as a bus attached hardware, and it self-operates such that any other block need not be in the operating mode, including the CPU. As mentioned above, to differentiate the concept of the power consumption techniques between the conventional and the proposed schemes, the authors distinguish between the terms dynamic and autonomous. Autonomous operations do not involve the intervention of the CPU or other processor. The conventional power management schemes have been mainly operated by software or firmware using the interrupt. For avoiding the additive running time of the program for interrupt service, measurement, estimation, and control, we propose an APM to perform clock control, DPM, and DVFS without the intervention of the CPU, unlike the conventional techniques, as shown in Fig. 2.



As shown in Figs. 2, the APM block implemented between the MP and the access control controls the PMIC to turn off the power supply to the system bus. A dedicated timer in the access control measures the periods of absence of the data from the MP. As soon as the requests for data read/write are completed, the timer is started to measure the periods.

If the periods exceed the threshold level, the power state is transited into the sleep mode for energy saving, as shown in Fig. 3. Subsequently, if new data requests for memory operation are available on the bus, the power is supplied to the power gated blocks. Simultaneously, the APM block holds the request until the memory interface block is completely recovered. The system bus with the memory controller consumes additional power in the wake-up mode and increases the latency as much as the wake-up time. Although sophisticated works on the PID controller, Kalman filter, various artificial intelligent algorithms, and particle filter have been presented from an OS perspective, they are inappropriate for DPM because the estimation methods involve computational workloads [7][8].

The implemented algorithm should be sufficiently light and simple to reduce the size and power consumption because DPM is an always-on block.

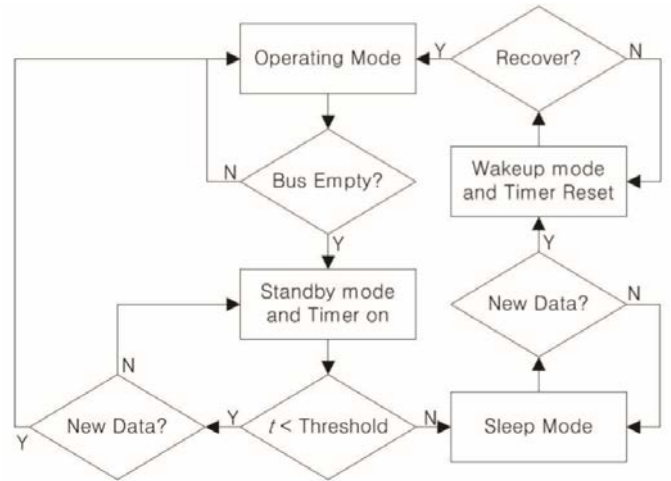


Fig. 3. Transition of power modes by autonomous power management.

The APM framework consists of an architecture to operate the DVFS or DPM controlled by hardware, a power management policy, and a control algorithm with measurement and estimation. Therefore, the APM can be adopted for the general-purpose system integrated with diverse IPs. It is possible to improve the performance of the system and to transit the CPUs from the active mode to the power saving mode because the function of the power management is distributed.

The power consumption can be controlled by the temperature, measurement of the data traffic, prediction of the workloads, or time constraints. The control algorithm of the APM is implemented by hardware or software for flexibility. However, the proposed APM controls the power gating on the basis of the periods between the requests. The details of the APM are presented in the next section.

In general, when the systems enter into the active mode from the power-saving mode, they have to wait for the stable power and clock to recover the systems. This waiting time is called the wake-up time. The power management policies need to consider the tradeoff between performance and power consumption because the wake-up time is significant, on the basis of the designed driving current of the power switch and its load capacitance. In other words, the objective of the power management policy is to determine the transit time for the power states and to determine the power state that should be discriminated by the conditions of the time constraints and workloads.

As listed in Table 1, there are three types of power management policies in the dedicated AP: Behavior1, Behavior2, and Behavior3. All the behaviors change the LPDDR memory from the functional mode to the self-refresh mode to save power. Behavior1 is a type of ACG with which the memory controller and delayed loop lock (DLL) block are autonomously transited into the clock-gated mode upon completing the memory operations. The transition time into the active mode depends on the frequency of the clock because the blocks need only one clock, which is small enough when compared with the other delays.

**Table 1. Power management policies for dedicated AP**

	<i>Behavior1</i>	<i>Behavior2</i>	<i>Behavior3</i>
Oscillator	ON	ON	P.G
Power switch	ON	P.G	P.G
PLL	ON	ON	P.G
Memory controller	C.G	P.G	P.G
Re-sync	ON	P.G	P.G
DLL (PHY)	C.G	P.G	P.G

C.G and P.G denote clock gating and power gating, respectively.

### III. SIMULATION RESULTS

To estimate the power consumption and performance by the proposed architecture, we performed the system-level simulation with high-level model, power model, traces of actual data traffic, and power management policy, as shown in Fig. 4. The virtual platform focuses on the system bus because the objective of this study is to develop an architecture for memory sharing.

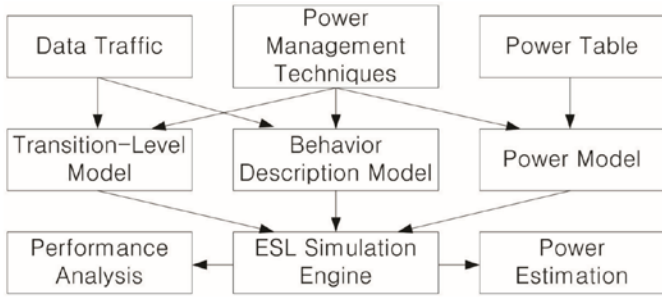


**Fig. 4** ESL simulation framework for performance analysis and estimation of power consumption.

One of the advantages of the system-level design is that the simulation can be adopted with the execution traces as an input. The traces have been obtained under the possible worst-conditions or depending on the practical situation of the user. Using the ESL environment for the verification of the performance and power consumption, the proposed architecture has been simulated and analyzed with the traces as an input. All the simulation inputs are generated under the worst-case conditions that users could possibly experience. First, the performance analysis of the proposed architecture is processed. Then, the power consumption is estimated.

After completing the performance analysis of the proposed architecture, the power consumption is evaluated for various scenarios. However, before devising an architectural design for APMs, the power consumption of the IMAP with sharing the memory exceeds that of the conventional architecture. The root cause is that the system bus is always operated for the memory operations of the MP block because the data pattern is nonuniform and sparse for communication between the UE and

the base station. In other words, the system bus cannot transit into the energy-saving mode because the arrival time of the data cannot be predicted. Therefore, various techniques including that using APMs have been proposed to support low-power voice communication. As mentioned in Section III, the transition time of the previous Behavior2 is 14  $\mu$ s, which depends on the load capacitance and driving current. The analog power switch is improved to shorten the wake-up time to 1  $\mu$ s because the policy violated the time constraint for voice communication.

With this improvement, we can guarantee a satisfactory time constraint for both idle and connected modes. Even in the idle mode, the improved Behavior2 is more effective than the previous Behavior3 because shortening the transition time is more effective than turning off the oscillator and PLL with a long wake-up time. In other words, the power consumption for the wake-up duration is very critical and cannot be ignored. The threshold time for Behavior2 of APM is determined to be 5  $\mu$ s, and the threshold time for Behavior3 is 5ms. However, the optimum solution for the threshold time has been presented in previous work[2]. Behavior1 and Behavior2 are autonomously operated by the hardware bus monitor. On the other hand, Behavior3 is processed by the software using the timers.

As shown in Figs. 5-8, power consumption is prevented during the standby mode because of APM. Although the multiple sleep states and thresholds are highly efficient in reducing the power consumption, the proposed architecture has selected only three thresholds for achieving the small size of the circuits and simple and light control.

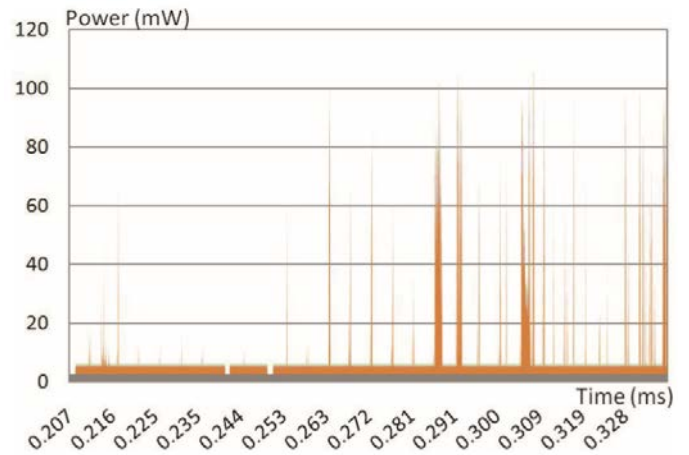


**Fig. 5.** Power consumption in idle mode of GSM by conventional Behavior3.

## IV. CONCLUSIONS

In this paper, an architecture for integrating the modem and the AP with the shared memory has been proposed. Furthermore, hardware-based DPM, APM is addressed for the time-constraint tasks such as wireless communication. In the case of voice communication, a specific policy for power management is proposed for agile and light operation without the intervention of CPUs because the data pattern is nonuniform and sparse. For evaluating the effectiveness and efficiency of the proposed architecture, a system-level simulation is performed for verifying the performance and power consumption. A simple and efficient power model and a power table are presented. The proposed APM is a new technique for reducing the power consumption without the use of software.

## REFERENCES

- [1] S.-H. Yang et al., "A 32nm high-k metal gate application processor with GHz multi-core CPU," in 2012 IEEE Int. Solid-State Circuits Conf. Digest of Tech. Papers, San Francisco, pp. 214-216.
- [2] S.-Y. Kim, K. Koo and S. W. Kim, "Time-based power control architecture for application processors in smartphones," Electron. Lett., vol. 48, no. 25, pp. 1632-1634, Dec. 2012.
- [3] USB 2.0 Supplement High-Speed Inter-Chip USB Electrical Specification Revision 1.0, USB Implementers Forum, Inc, 2007.
- [4] MIPI Alliance, Low Latency Interface Specification. [Online] Available: <http://www.mipi.org/lli>
- [5] V. Hanumaiah, S. Vruthula, and K. Chatha, "Performance optimal online DVFS and task migration techniques for thermally constrained multi-core processors," IEEE trans. Comput.-Aided Des. Integr. Circuits Syst., vol. 30, no. 11, pp 1677-1690, Nov. 2011.
- [6] S. Jahagirdar et al., "Power management of the third generation Intel core micro architecture formerly codenamed Ivy Bridge," presented at the Hot Chips 24, Cupertino, CA, Aug. 2012.
- [7] H. S. Lee and B. K. Kim, "Design of digital control systems with dynamic voltage scaling", in 2004 IEEE Proc. Real-Time and Embedded Technology and Applications Symp., pp. 94-101.
- [8] J.-B. Lee et al., "Application-support particle filter for dynamic voltage scaling of multimedia applications," IEEE trans. Comput., vol. 61, no. 9, pp. 1256-1269, Sep. 2012.

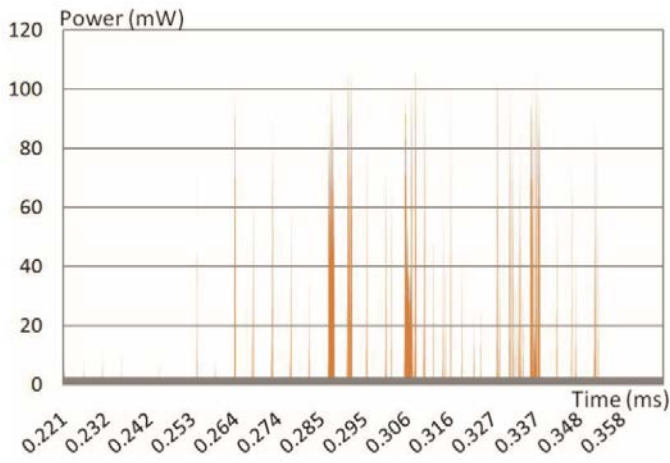


Fig. 6. Power consumption in idle mode of GSM by proposed Behavior2.

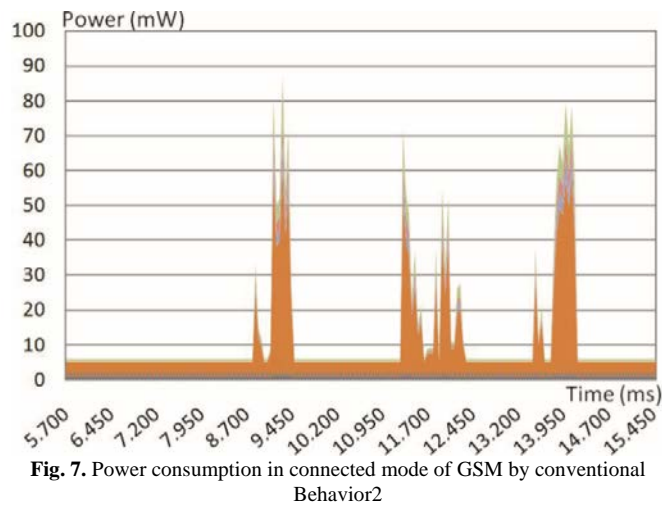


Fig. 7. Power consumption in connected mode of GSM by conventional Behavior2

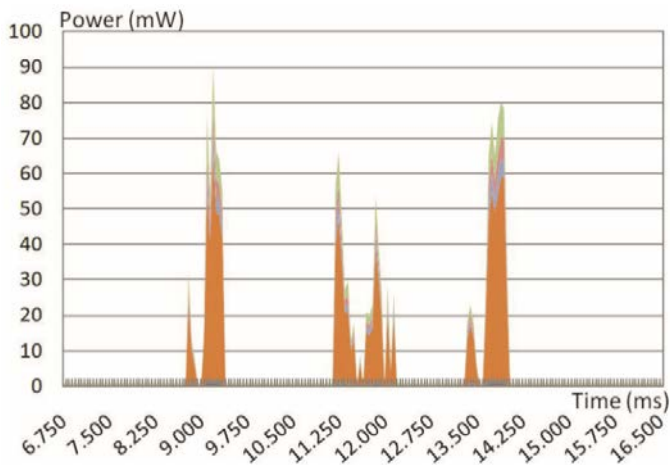


Fig. 8. Power consumption in connected mode of GSM by proposed Behavior



# Construction and evaluation of three-dimensional archive of cultural contents

Hayoung Yoon

Digital Contents Design department  
Osan University  
Osan-si, Republic of Korea  
yoon@osan.ac.kr

Jihun Koo

Smart IT department  
Osan University  
Osan-si, Republic of Korea  
Jihun.koo@osan.ac.kr

**Abstract**—In this study produced a stereoscopic archive for the heritage of industrial modernization, which was dismantled in March 2011, by converting the 2D images to 3D, and examined the impressions. Moreover, the drawing images of the cultural asset were also converted to 3D images in order to evaluation the expression as a stereoscopic archive. For the experiment, head mounted display and 42-inch 3D TV were used. 30 students in twenties years of age. with normal binocular vision. participated through questionnaires and interviews to compare the impressions, between the conditions.

**Keywords**— *Stereoscopic images, cultural contents, 2D to 3D conversion, human factors*

## I. INTRODUCTION

The heritage from the period of industrial modernization is considered part of the cultural heritage in Japan. This includes buildings fundamental to Japanese modernization such as steelworks and dockyards, as well as facilities that have contributed to modernization, such as river facilities or harbors[1].

The Japanese Ministry of Economy, Trade and Industry defined historical buildings or machinery with cultural value in terms of history and the economy as “Heritage of Industrial Modernization” in 2007. Five hundred and seventy-five relevant heritage items have been registered. In 2008, an additional 540 items in the machine and chemical industries were added to the register for the purpose of local revitalization. Specifically, the selection of items that constitute the heritage of industrial modernization was divided between the “Heritage Group of Industrial Modernization 33” and the “Sub-Heritage Group of Industrial Modernization 33” according to their relevancies to specific local and industrial histories. [2]Currently, each of these is regarded as a valuable Japanese cultural asset that has played a part in fundamental modernization and preserves the economic and historical values of relevant industrial facilities.

However, structural defects arising from natural disasters or deterioration sometimes force registration cancellation or cause disintegration of the physical structure. However, this problem is not confined to industrial modernization heritage. It is a

common problem shared by numerous tangible cultural assets. Therefore, research has been carried out in terms of digitalization for semi-permanent preservation of cultural assets. In addition, there has been active research into the recording of cultural assets using stereoscopic (3D) image technology, known as a “stereoscopic archive” [3].

A stereoscopic archive records and preserves the depth information of an object's structure and shape. Therefore, it considered adequate for recording large-scale objects

such as buildings and tangible objects such as landscapes [4]. However, recording and preserving a disintegrated building using three-dimensional images is not possible because three-dimensional camera shooting is not available. This problem can be resolved with technology that simulates binocular vision, i.e., 2D to 3D conversion. The 2D to 3D conversion technology expresses a 2D image in 3D through an automatic or manual imaging process. It has been widely used recently in the 3D content production industry. The process is carried out after image shooting is completed so that visual expressions become available based on accumulated conventional 2D content production knowhow [5]. However, there have been inadequate discussions on audience impressions of contents converted by 2D to 3D conversion, in comparison to that of 2D contents.

## II. PURPOSE

While the 2D to 3D conversion technology mentioned in the previous section has been widely used in the 3D production industry, use of the 2D to 3D conversion in stereoscopic archive content production, which records the structure and shape information of a cultural asset, is not yet established.

This study built a stereoscopic archive for the JVC KENWOOD Yokohama Plant, which has been registered as an industrial modernization heritage site, using 4K2D imaging to record the structure and shape of the cultural asset, followed by an evaluation of its impression change with audiences. Moreover, an evaluation of the simultaneously expressed senses of scale and presence was intended for the 3D data of the cultural asset building drawings, which contain only 2D information, as an approach to record the cultural asset.

### III. BUILDING THE STEREOSCOPIC ARCHIVE

4K2D materials taken and supplied by JVC KENWOOD and the building drawing data were used as the 2D image sources for building the stereoscopic archive.

The object was the JVC KENWOOD (JVC) Yokohama Plant (Figure 1). A reinforced concrete building completed in 1930, it was designed by the Mitubisi Limited Partnership Company (currently Mitubisi Zisyo). In this study, the focus was placed on the central part of the facility, the façade, for the stereoscopic archive of the factory. Though most of the façade facility was lost in 1945 due to the war, a portion of it was well-preserved as the plant entrance building and became the symbol of the factory. This iconic architecture, having a classical building column structure, was rare and precious for a factory building. However, the building was demolished in January 18, 2011 when the factory was sold [6].



Figure 1. Yokohama JVC KENWOOD Factory (left) and the façade (right)

JVC considered moving the building itself, since this historical building could not be preserved at its original location due to disposal of the Yokohama factory facilities. However, they finally decided to demolish the building because the building had seriously deteriorated and likely to collapse. Otherwise, extensive earthquake resistant reinforcement would be required. Subsequently, JVC and the City of Yokohama agreed to restore the building in the future and conducted image shooting of the building, preparing building drawings, and storage of partial building materials.

They recognized the importance and necessity of recording and preserving the Yokohama JVC factory's façade as a stereoscopic archive for future restoration.

Our stereoscopic archive 3D contents were constructed using 4K2D images and the building drawings prepared as part of the restoration activities. The production was progressed in the following order: ① 3D design and story configuration, ② 2D to 3D conversion, ③ 3D editing, ④ evaluation of the 3D contents, and ⑤ completion.

① The design and story constitution for each scene are described. Each scene is depicted in Figure 2 (Figure 2). In the first scene, the title, "Yokohama JVC Plant Stereoscopic Archive" is displayed, followed by an introduction of the plant. The second scene shows the bird's eye view of the plant while the factory is closely zoomed up. In the third scene, the camera is traveling from the rear factory gate to the front gate to show the entire factory facilities. The façade is closely investigated in the fourth and fifth scenes. Magnified images of the façade are subsequently shown in the sixth and seventh scenes. For

instance, building columns and handles were brought up, followed by showing the building drawings in 3D to grasp each building component's structure and shape. Finally, the eighth scene zooms the monument out and brings up the credit titles. The total playing time from the first scene to the eighth scene is 2 minutes and 51 seconds.

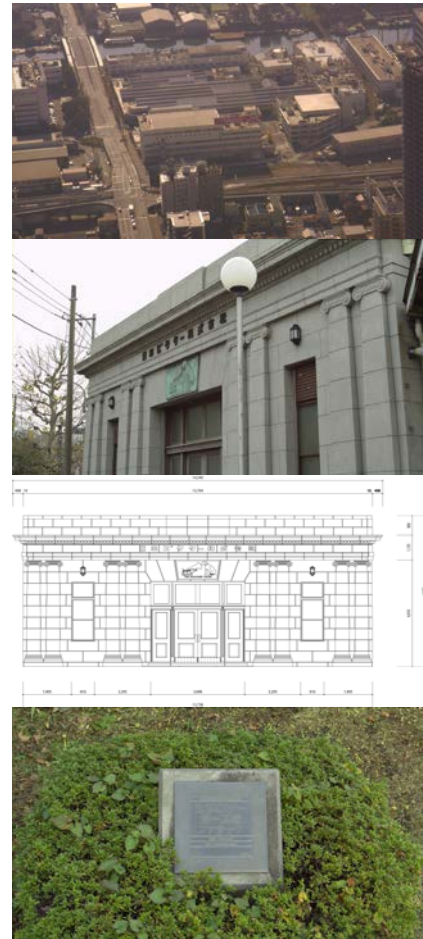


Figure 2. Flow of stereoscopic archive content

The total playing time from the first scene to the eighth scene is 2 minutes and 51 seconds. ② The 2D image was then converted to a 3D image by providing binocular vision information using the 2D to 3D conversion technology. This technology is generally used to convert an image prepared in 2D to a 3D image or to complement some defects in a 3D image prepared by a stereoscopic camera. Though stereoscopic shooting has improved and is able to produce 3D images, depth expression with the correct sequence is still unable to reproduce the 3D characteristics of huge buildings, bird's eye views, and deep forests.

However, 2D to 3D conversion deals with images shot by 2D cameras, so directing 3D images can be readily done. Moreover, it is also advantageous because no expensive equipment, such as a 3D camera, is needed. The critical point of 2D to 3D conversion for realizing an actual space is to understand the

object's spatial arrangement. 2D to 3D conversion methods are depicted in Figure 3. First, a depth map that visualizes relevant depth information is prepared with a 2D image. The depth map is generally shown in a 256-color grey scale image expressing depth and distance using colors. The image depth is rearranged in a coordination system using the information, followed by rendering of the left and right images in order to show a stereoscopic picture [7] [8].

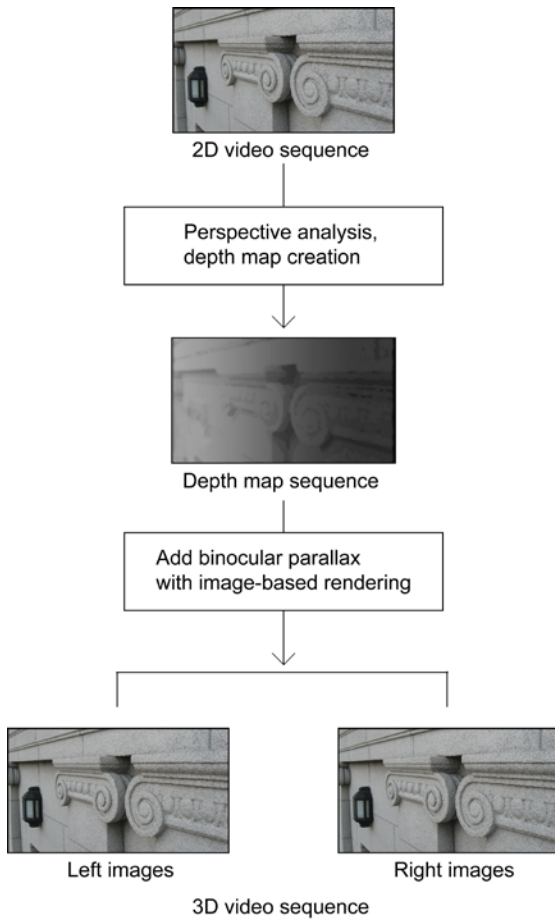


Figure 3. Order of 2D to 3D conversion

#### IV. EVALUATION OF 3D ARCHIVE CONTENTS

An image was prepared for evaluation with the stereoscopic archive contents. Specifically, the video included the building image (1 minute and 30 seconds) and the image from building drawings (1 minute 30 seconds) with a resolution of  $1920 \times 1080$  pixels with a top and bottom type.

The following eight conditions were applied to the contents (building images and drawing images) and the types of images (2D and 3D) in order to carry out an experiment with the displays (HMD and TV) (Table 1.) The experimental procedures were performed in the following order. ① Questionnaire explanations, test procedures, and HMD were

provided in the preparatory stages of the experiment. ② Conditions were randomly suggested. ③ Participants were then asked to complete the questionnaire and interviewed. The eight conditions were evenly applied using the methods. The experiment was carried out in sixty minutes, including the preparatory session. The experiment was carried out in a dark room, to block light in the experimental environment. The experimental environments are depicted in Figure 6. Thirty students in their twenties with normal color vision and binocular vision were selected as subjects.

Table 1. Experimental conditions

Display	Contents	Types of image	Condition
TV	Building	2D	TV-B2D
		3D	TV-B3D
	Building drawing	2D	HMD-P2D
		3D	HMD-P3D
HMD	Building	2D	TV-B2D
		3D	TV-B3D
	Building drawing	2D	HMD-P2D
		3D	HMD-P3D

#### V. RESULTS AND DISCUSSION

Multiple comparisons based on “Bonferroni” were conducted after carrying out variance analyses for three factors, including the display (TV and HMD conditions), the contents (building (B) and building drawing (P) conditions), and the types of image (2D and 3D conditions).

Each questionnaire item was also evaluated, including 3D effects, presence, a sense of scale, visually induced motion sickness, and interest level. First of all, the question for presence was analyzed. Significant differences were observed between Question 3, “Naturalness of image” and Question 7, “Ease of image” in terms of the main effect of the image types, which were ( $F(1,29) = 10.191, p < .05$ ) and ( $F(1,29) = 14.485, p < .01$ ), respectively, while the differences between the display and the contents were not significant in terms of the main effect. On the other hand, significant differences ( $F(1,29) = 189.424, p < .01$ ) were observed for Question 4, “Image depth”, between two image types, as well as significant differences ( $F(1,29) = 4.880, p < .05$ ) between contents and image types, so that multiple comparisons were conducted (Figure 7). However, no significant differences were seen between displays in the questions relevant to 3D effects. The significance of contents and image types were recognized. As the average points were analyzed, the 3D condition points were determined to be more significant, so that the higher reliability of stereoscopic content reproducibility when prepared by 2D to 3D conversion was confirmed.

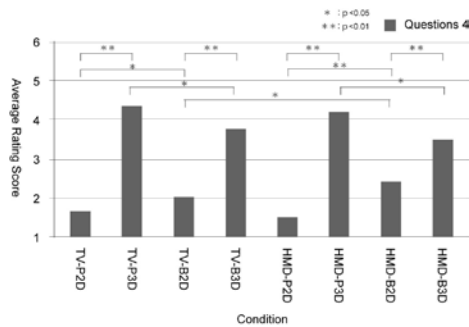


Figure 7. Items relevant to the 3D effect

The significant difference ( $F(1,29) = 10.487, p < .01$ ) of the main effect for the display in Question 8, “I feel I am at the actual place”, which is relevant to presence, was recognized, as well as the significant difference for the contents ( $F(1,29) = 13.718, p < .01$ ) and that of the image types ( $F(1,29) = 32.648, p < .01$ ), respectively.

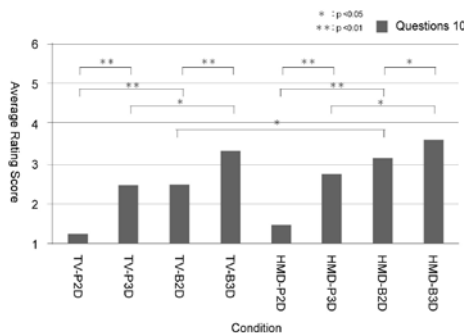


Figure 8. Items relevant to the presence

Moreover, the simple interaction between the displays and the contents turned out to be significant ( $F(1,29) = 8.534, p < .01$ ) and the difference between TV-B3D and HMD-B3D as well as between TV-B2D and HMD-B2D were significant after multiple comparisons. Furthermore, the significance of the main effects between displays, contents, and image types was also recognized for Question 10, “It has a sense of reality”. At the same time, the simple interaction between the contents and the types of image was also significant ( $F(1,29) = 6.853, p < .05$ ). Details are summarized in Figure 8.

For the questions relevant to presence, the significance of the main effects for each factor was recognized. HMDs received higher average points than TVs; therefore, the HMD characteristics are assumed to positively influence presence. Moreover, many participants answered positively, such as, “I could easily focus on the image” and “It has a sense of reality”. On the other hand, some subjects complained about pain and fatigue arising from the weight or the wearing of the HMD, so looking at the image for a long time with HMD may not be appropriate. Next, the average rate point of Question 1, “I could easily understand the building structure”, relevant to the sense of scale is depicted in Figure 9. The significance of the main effects on the image types was observed in the sense of scale.

The interviewees had positive reactions, such as “I could understand the building structure” and “I could imagine the building size”. This means that the impression of the building shape, size, and sense of scale were positively affected by the 3D effect. Meanwhile, the displays and the content factor did not directly influence the sense of scale. ( $F(1,29) = 61.780, p < .01$ ), but the main effects and interaction between the displays and the contents were not recognized. the sense of scale is depicted in Figure 9. The significance of the main effects on the image types was observed in the sense of scale ( $F(1,29) = 61.780, p < .01$ ), but the main effects and interaction between the displays and the contents were not recognized

## VI. CONCLUSION

In the questionnaire evaluation results, the 3D conditions were highly valued in the items relevant to a sense of scale. Therefore, the effectiveness of stereoscopic archive contents was confirmed in expressing the structures and atmosphere of a cultural asset through 2D to 3D conversion. Moreover, conversion of building drawings with mere 2D information to 3D images was assumed to have positive effects on promoting the grasping of building scale with minimum disharmony. For the impression change of contents by the displays, TVs were highly valued for elements relevant to 3D effects, while HMDs were positively evaluated for elements relevant to presence and interest level. The results imply that the characteristics of HMDs are effective at positively expressing presence in terms of content impression changes. On the other hand, some audiences experienced eye fatigue and visually induced motion sickness because the screen is coupled with head movement, meaning that the viewing conditions or wearing methods of the device require further consideration.

## REFERENCES

- [1] Tamada, H. and Matsuoka, K., “Architecture and analysis of the gis database of industrial heritages in kyoto city,” Architectural Institute of Japan, Papers 14(28), 617-620 (2008) (in Japanese).
- [2] Ministry of Economy Japan., “33 Heritage Constellations of Industrial Modernization vol.2,” October 2008, <<http://www.meti.go.jp/press/20090206001/20090206001-2.pdf>> (October 2008) (in Japanese).
- [3] Ikeuchi, K., Hasegawa, K., Nakazawa, A., Takamatsu, J., Oishi, T. and Masuda, T., “Bayon Digital Archival Project”, Proceedings of the Tenth International Conference on Virtual System and Multimedia. Papers 334-343, (2004).
- [4] Kawai, T., Takao, H., Inoue, T., Miyamoto, H. and Noro, K., “Virtual museum of Japanese-Buddhist temple features for intercultural communication,” Proc. SPIE 3295, 144-147 (1998).
- [5] Kawai, T., Shibata, T., Mochizuki, T. and Noro, K., “Production of stereoscopic 3D movies of a Spanish monastery for a digital archive,” Proc. SPIE 3957, 284-287 (2000).
- [6] Grauer, R., “A Role and Responsibility for Media in the Future of Traditional Arts,” Proc. Symposium on Preservation and Promotion of Asian Traditional Performing arts, 88-99 (2000).
- [7] Abe, N., Ohta, K., Kawai, T., Ando, K., Kakinuma, T., Fujita, K. and Kudo, N., “evaluation of stereoscopic contents for a museum exhibition,” Journal of Information Display. Papers 12(3), 159-165 (2011).
- [8] Kawai, T., Kishi, S., Yamazoe, T., Shibata, T., Inoue, T., Sakaguchi, Y., Okabe, K., Kuno, Y., Kawamoto, T., “Ergonomic evaluation system for stereoscopic video production,” Proc. SPIE 6055, 60551B (2006).



# Optimization of Magnetic Resonance Wireless Power Transfer System in Concrete Structures

Ji-min Kim<sup>1)</sup>

<sup>1)</sup> Department of Civil and Environmental Engineering

<sup>1)</sup> Korea Advanced Institute of Science and Technology

<sup>1)</sup> Daejeon, Korea

<sup>1)</sup> [jimin.kim@kaist.ac.kr](mailto:jimin.kim@kaist.ac.kr)

Ho-sik Park<sup>2)</sup>, and Minseok Han<sup>2)</sup>

<sup>2)</sup> Department of Electronics

<sup>2)</sup> Osan University

<sup>2)</sup> Gyeonggi-do, Korea

<sup>2)</sup> [mshan1024@osan.ac.kr](mailto:mshan1024@osan.ac.kr) (corresponding author)

**Abstract**— Power management is critical for operating wireless sensors. In particular, the wireless sensor used for continuous monitoring of civil infrastructure is often installed on the location that is difficult to access, and the expected lifespan of these sensors exceeds that of conventional batteries. In spite of outstanding capability for damage identification, many conventional structural health monitoring (SHM) techniques are restricted to cover huge structures because of their wired system for data and power transmission. Recently, though the advent of wireless data transmission through radio-frequency technique made a breakthrough for a new stream of wireless sensors in SHM, power supplying issue is still unsolved. Normal battery cannot endure a whole life span of general civil infrastructures more than a few decade. This study optimizes magnetic resonance based wireless power transmission system and its performance is validated in three different mediums: (1) air, (2) unreinforced concrete and (2) reinforced concrete. The effect of concrete and steel rebar is observed and analyzed.

**Keywords**- Magnetic resonance, reinforced concrete, structural health monitoring, wireless power transfer.

## I. INTRODUCTION

Wireless sensor networks (WSNs) for structural health monitoring (SHM) applications can allow for a rapid assessment of structural integrity after an event such as a natural disaster puts the reliability of civil infrastructure. SHM techniques using various sensors such as accelerometer, strain sensor and piezoelectric sensor were investigated and their performances are already validated by continuous studies [1-3]. However, expensive and heavy wiring system of each sensor to transfer monitoring data and power restricts to be employed for large civil infrastructures. In recent, wireless sensors for SHM has been taken attention and notable progress of wireless data transmission techniques boosted the development of wireless sensor [4-5]. However, operation of a wireless sensor mainly relies on limited battery power and capacity of the battery cannot support to power the wireless sensor during a whole lifespan of civil infrastructures more than a few decades in general.

A new powering strategy is highly required to use the wireless sensor. As an alternative, researchers suggested energy harvesting which can harness energy through surrounding environment such as vibrations and natural lights [6-8]. Energy

harvesting is considered as a promising technique to power wireless sensor without human labor after initial installation. However, the amount of the collected energy from a few  $\mu\text{W}$  to  $\text{mW}$  is not sufficient to operate the wireless sensor and specific conditions should be satisfied to store the optimum level of energy. On the one hand, wireless power transmission (WPT) technique has been considered as another alternative, thanks to the following advantages: (1) larger amount of power can be supplied and (2) whenever it is required, power can be transferred to the wireless sensors.

In recent, Kurs (2007) proposed a WPT technique using magnetic resonance [9]. Comparing with well-known inductive coupling based WPT [10-11], this technique can transfer power to a distance of hundreds of millimeters in high power transmission efficiency (PTE). After that, many related studies have been progressed to increase transmission distance and efficiency through air [12-14]. Jonah (2013) examined PTE through concrete and reinforced concrete (i.e., concrete with rebars) which is inhomogeneous medium [15]. While examination of PTE change induced by thickness and humidity variation of concrete was successful, analysis of concrete and steel rebar effects is still insufficient. In this study, magnetic resonance based wireless power transmission technique is investigated. Resonance coils of 6.78 MHz are optimally designed to achieve high Q-factor and coil-to-coil PTE is experimentally measured and compared for three different conditions: (1) air, (2) unreinforced concrete and (3) reinforced concrete. The effects of concrete and steel rebar are analyzed to PTE change.

In this paper, magnetic resonance based wireless power transfer technique is investigated. Resonance coils of 6.78 MHz are optimally designed to achieve high Q-factor and coil-to-coil PTE is experimentally measured and compared for three different mediums: (1) air, (2) unreinforced concrete and (3) reinforced concrete. The effects of concrete and steel rebar are analyzed to PTE change.

Section 2 explains fundamental principles of magnetic resonance based WPT and section 3 describes resonance coil design procedures. PTE of the designed resonance coils is evaluated and compared for different mediums in section 4. Brief summary and future works are offered in section 5.

## II. WIRELESS POWER TRANSMISSION USING MAGNETIC RESONANCE

Magnetic resonance based WPT (MR-WPT) is mid-range WPT technique aiming to achieve power transmission distance more than tens of centimeters.

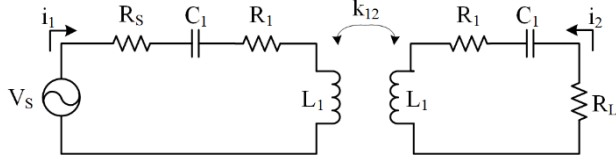


Fig. 1. A circuit model of magnetic based wireless power transmission

Fig. 1 is a simplified circuit model of MR-WPT consisting of transmitting (Tx) coil, receiving (Rx) coil, power source and load. Two resonance coils of same resonance frequency are coupled through magnetic field between them and energy of the power source is transferred to the load through the magnetic field between Tx coil and Rx coil [15-17]. The coupling coefficient between resonance coils can be expressed as follows:

$$k_{12} = \frac{M_{12}}{\sqrt{L_1 L_2}} \quad \text{Eq. (1)}$$

$L_1$ ,  $L_2$  and  $M_{12}$  are self-inductance of each coil and mutual inductance, respectively.  $k_{12}$  represents the strength of magnetic coupling between Tx and Rx resonance coils.

$$\begin{bmatrix} V_s \\ 0 \end{bmatrix} = \begin{bmatrix} Z_1 & j\omega M_{12} \\ j\omega M_{12} & Z_2 \end{bmatrix} \begin{bmatrix} i_1 \\ i_2 \end{bmatrix} \quad \text{Eq. (2)}$$

Eq. (2) is node equation of the circuit mode in Fig. 1.  $V_s$  is input voltage from the power source and  $\omega$  is the designated resonance frequency of coil.  $i_1$  and  $i_2$  denote current through Tx and Rx circuits, respectively.  $Z_1$  and  $Z_2$  means impedance of each circuit and they can be calculated by Eqs. (3):

$$\begin{aligned} Z_1 &= R_s + R_1 + j\left(\omega L_1 - \frac{1}{\omega C_1}\right) \\ Z_2 &= R_L + R_2 + j\left(\omega L_2 - \frac{1}{\omega C_2}\right) \end{aligned} \quad \text{Eq. (3)}$$

$R_1$ ,  $R_2$ ,  $R_s$  and  $R_L$  are resistances of Tx coil, Rx coil, power source and load, respectively. And  $C_1$  and  $C_2$  represent capacitance of Tx and Rx coils.

When solving Eq. (2) and Eqs. (3) against  $i_2$ , load voltage,  $V_L$ , is computed as following Eq. (4):

$$V_L = -i_2 \cdot R_L = \left( \frac{V_s \cdot (j\omega M_{12})}{Z_1 Z_2 + \omega^2 M_{12}^2} \right) \cdot R_L \quad \text{Eq. (4)}$$

When the system is supposed as a simple two port network, the amount of transmitted power can be quantified using transmission coefficient,  $S_{21}$ , of S-parameter [15, 17]. As shown in Eq. (5),  $S_{21}$  can be acquired using the electric components of the circuit model and PTE ( $\eta$ ) of the proposed MR-WPT is produced by Eq. (6):

$$S_{21} = 2 \frac{V_L}{V_s} \left( \frac{R_s}{R_L} \right)^{1/2} = \frac{j\omega M_{12} \sqrt{R_s R_L}}{Z_1 Z_2 + \omega^2 M_{12}^2} \quad \text{Eq. (5)}$$

$$\eta = |S_{21}|^2 / (1 - |S_{11}|^2) \times 100 (\%) \quad \text{Eq. (6)}$$

## III. OPTIMIZATION OF RESONANCE COILS

Design of resonance coils is one of the most significant procedure to maximize PTE.

$$Q = \frac{\omega L}{R} \quad \text{Eq. (7)}$$

$Q$  is a calculated Q-factor of a coil and  $\omega$  is a resonance frequency.  $L$  and  $R$  denote self-inductance and resistance of the coil, respectively. Since PTE of the system ( $\eta$ ) is directly related with its Q-factor, it is essential to realize maximum Q-factor under same geometric restrictions and the relationship between them is provided in Eq. (8).

$$\eta = \frac{1}{1 + \frac{1}{k^2 Q_1 Q_2}} \cdot \frac{R_L}{R_2 + R_L} \quad \text{Eq. (8)}$$

$Q_1$  and  $Q_2$  are Q-factor of Tx and Rx coil, respectively, and  $k$  is coupling coefficient between them. The  $R_2$  denotes resistance of Rx coil and  $R_L$  means load resistance.

Optimization of resonance coils are one of the most significant procedures to maximize PTE. Since higher Q-factor of resonance coil means higher PTE, it is essential to realize maximum Q-factor under same geometrical restrictions.

$$Q = \frac{\omega L}{R} \quad \text{Eq. (9)}$$

$Q$  is a calculated Q-factor of a coil and  $\omega$  is a resonance frequency.  $L$  and  $R$  denotes inductance and resistance of the coil.

Table. 1 shows the detailed design parameters of each Tx and Rx resonance coil. An equivalent circuit model of MR-WPT system is shown in Fig. 2. The primary circuit is modeled as an AC voltage source with an amplitude of  $V_s$  and a source impedance of  $Z_s$ , and the secondary circuit is represented by a load impedance of  $Z_L$ . The resonant frequency,  $f$ , of Tx and Rx resonators can be expressed as follows and tuned by adjusting equivalent lumped  $L$  and  $C$  values.

Table 1. Detailed design parameters of each Tx and Rx resonance coil and Equivalent circuit

	Tx coil	Rx coil
Diameter	330 mm	330 mm
Number of turns	7 turns	7 turns
Wire diameter	2.28 mm	2.28 mm
Pitch	2.28 mm	2.28 mm
R	0.2 Ohm	0.2 Ohm
L	30.3 $\mu$ H	29.7 $\mu$ H
Cs	280 pF	280 pF
Cp	3.3 nF	4.7 nF

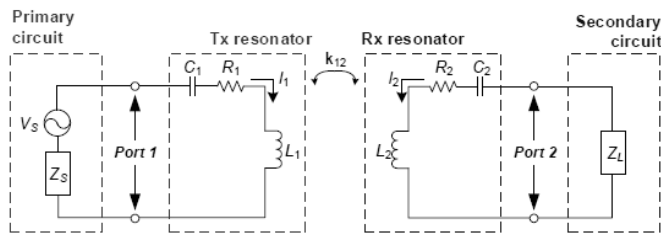


Fig. 2 Equivalent circuit model

Fig. 3 is the manufactured resonance coil according to the design parameters determined by previously mentioned steps.

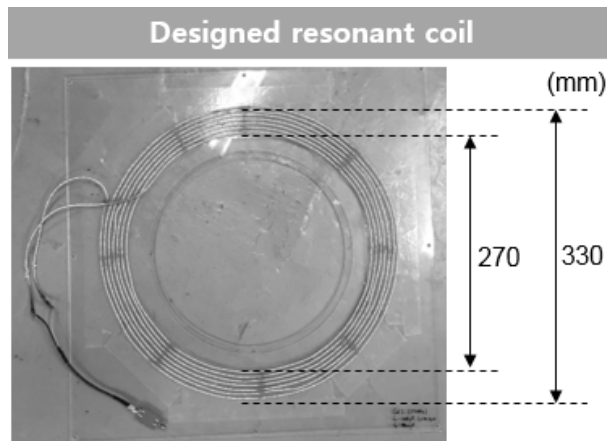


Fig. 3. Manufactured resonance coil according to the design parameters

#### IV. RESULTS AND DISCUSSIONS

In section 4, PTE of the designed resonance coils are experimentally measured for three different conditions: (1) air, (2) unreinforced concrete and (3) reinforced concrete. By comparing PTE changes of each condition, the effects of concrete and steel rebar to PTE are analyzed. Two concrete structures are specially designed. One is unreinforced concrete

and the other is reinforced concrete. The mix proportioning and detailed geometrical information are shown in Table 2 and Table 3. In particular, not only the concrete thickness, spacing of steel rebar but also compressive strength are determined under the consideration of real concrete bridge construction.

Table 2. Mix proportioning for concrete structures

Gradients	Unit Weight (kg/m <sup>3</sup> )
Cement	480
Water	164
Sand	778
Gravel	869
WRA	58.9

Table 3. Geometric information of concrete structures

Geometric information	Value
Concrete size (W $\times$ H $\times$ T)	600 $\times$ 600 $\times$ 300 mm <sup>3</sup>
Diameter of steel rebar	15 mm
Spacing of steel rebar	150 mm

Blueprints of the manufactured concrete structures are shown in Fig. 4. Concrete size is 600 mm 600 mm 300 mm and steel rebar is placed at 50 mm distant from the bottom.

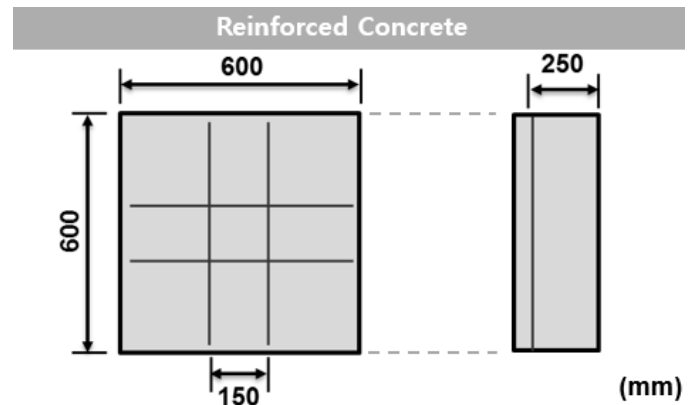
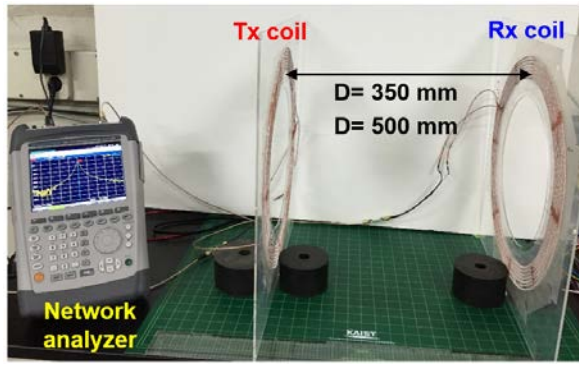
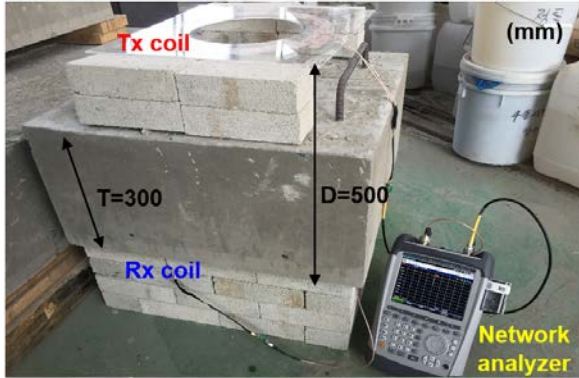


Fig. 4. Blueprints of reinforced concrete

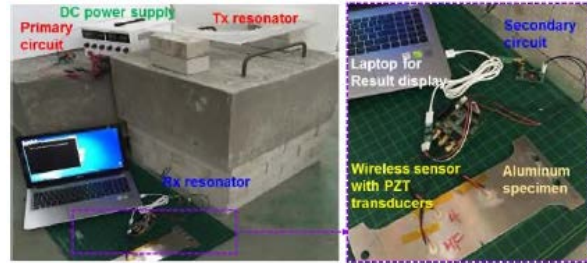
Experimental setup is shown in Fig. 5. For both air and concrete conditions, Tx and Rx coils are placed at the top and bottom, respectively and the distance between them are fixed as 330 mm. In particular, Tx and Rx coils are 15 mm distant from the top and bottom surface of concrete.



(a) Through air



(b) Through concrete



(c) operating a wireless sensor crack detection

Fig. 5. Experimental setups for PTE measurement using MR-WPT through air and concrete structures, and operating a wireless sensor for fatigue crack detection

Reflection coefficients ( $S_{11}$ ,  $S_{22}$ ) at Tx and Rx coils and transmission coefficients ( $S_{21}$ ) are measured and the results are shown in Figs. 6, 7 and 8. While  $S_{11}$  and  $S_{22}$  clearly have a single peak in air condition, splitting phenomena happens when concrete is closely place to Tx and Rx coils. Comparing PTE of each condition in Fig. 9, existence of concrete decreases PTE over broader frequency range. In spite of the expected reflections and attenuations of electromagnetic wave caused by concrete structure, concrete brings about decreasing of PTE comparing with air condition and it is speculated that the degree of this effects depends on the dielectric properties determined by mix proportioning. On the other hand, steel rebar which is conductor definitely induces degradation of PTE because of reflections and eddy currents at its surface.

In fact, PTE of reinforced concrete is approximately 20 % lower than that of unreinforced concrete in experiment. The input power is 16.27 W and 19.84 W at  $D = 450$  mm and  $D = 500$  mm, respectively, and the received power is 3.43 W. Finally, the overall system PTE is measured to be 21.34% at  $D = 450$  mm and 17.29% at  $D = 500$  mm.

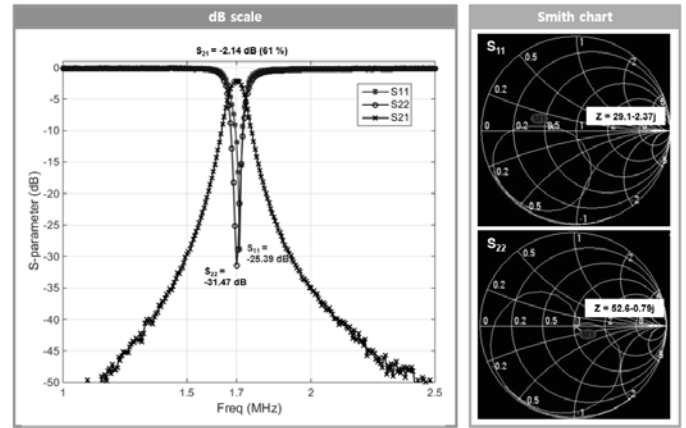


Fig. 6. Measured S-parameter characteristics through air ( $D=350$  mm)

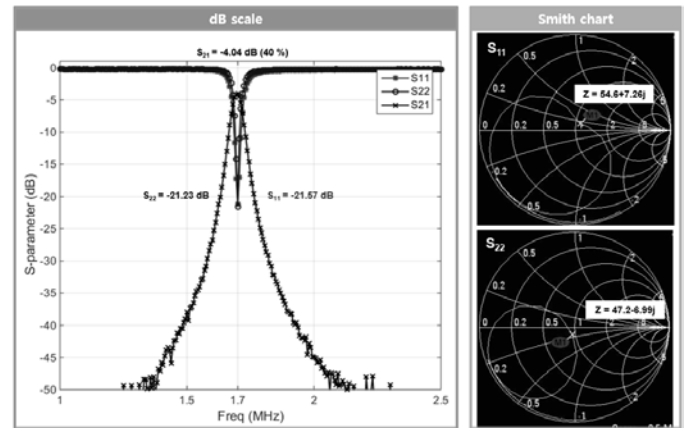


Fig. 7. Measured S-parameter characteristics through air ( $D=500$  mm)

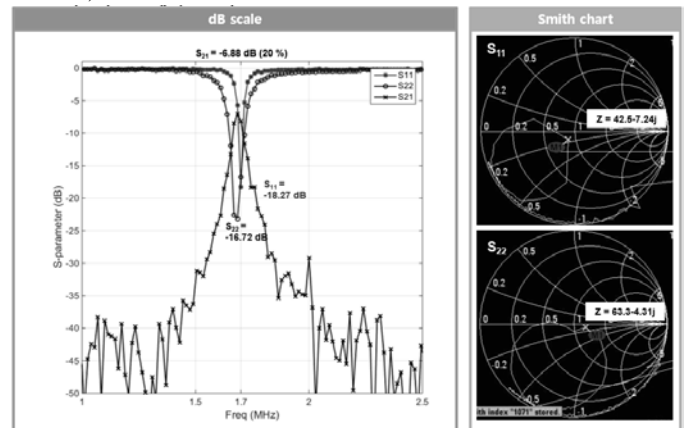


Fig. 8. Measured S-parameter characteristics through concrete ( $D=500$  mm)



## V. CONCLUSIONS

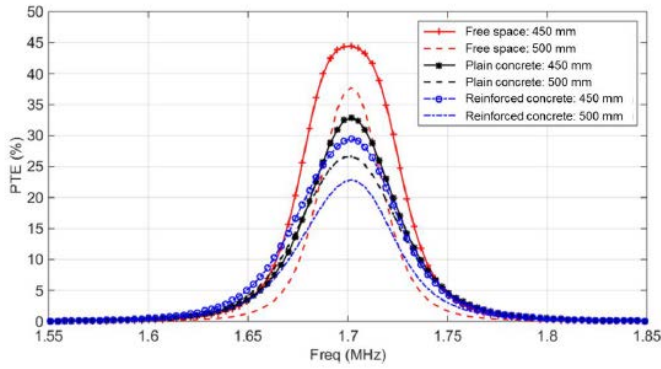


Fig. 9. PTE variations between Tx and Rx resonators through: (1) free space, (2) plain concrete and (3) reinforced concrete

While PTE only between Tx and Rx resonators is measured in Fig. 9, Table 4 shows PTE of the all system additionally considering (1) power consumption of the electric components in the primary and the secondary circuits, and (2) EM wave reflection because of impedance mismatch between the circuits and the resonators. The transmitted power is measured through reinforced concrete after replacing the wireless sensor with 5 ohm cement resistor. The input power is 16.27 W and 19.84 W at D=450 mm and D=500 mm, respectively, and the received power is 3.43 W. Finally, the overall system PTE is measured to be 21.34 % at D=450 mm and 17.29% at D=500 mm.

Table 4. The overall system PTE of the developed MR-WPT system through the reinforced concrete structure at D=450 mm and D=500 mm

	D=450mm	D=500mm
Input Power (W)	16.27	19.84
Output Power (W)	3.43	3.43
System efficiency (%)	21.34	17.29

In this paper, the effects of concrete and steel rebar to PTE was examined in application of MR-WPT. Resonance coil of 6.78 MHz frequency was analytically designed to produce maximum Q-factor. Unreinforced and reinforced concrete were specially designed following construction conditions of real concrete bridges. PTE was measured and compared for three different conditions: (1) air, (2) unreinforced concrete and (3) reinforced concrete. Despite of reflections and attenuations of electromagnetic waves by concrete, existence of concrete induces improvements of PTE. Concrete affects the generation of magnetic field between resonance coils and the detailed interactions is worth to investigate in following research. As comparing the results of unreinforced and reinforced concrete, it is proved that steel rebar of 150 mm spacing causes degradation of PTE less than 20 %. This study showed that MR-WPT is promising technique to power wireless sensors for SHM of concrete structure. In future, independent MR-WPT system will be developed including amplifying and rectifying circuits and applied to power wireless sensors in use. And finally, applicability of the developed MR-WPT system for in-service reinforced concrete structures will be experimentally validated.

## REFERENCES

- [1] H.J. Lim, H. Sohn and P. Liu, "Binding conditions for nonlinear ultrasonic generation unifying wave propagation and vibration", *Applied Physics Letters*, vol. 104, no. 21, 214103, May. 2014
- [2] A. Sophian, G.Y. Tian and S. Zairi, "Pulsed magnetic flux leakage techniques for crack detection and characterization", *Sensors and Actuators A: Physical*, vol. 125, pp. 186-191, Aug. 2005
- [3] S. Wagle and H. Kato, "Ultrasonic detection of fretting fatigue damage at bolt joints of aluminum alloy plates", *International Journal of Fatigue*, Vol. 31, no. 8-9, pp. 1378-1385, Aug. 2009
- [4] S. Cho, S.A. Jang, H. Jo, J.W. Park, H.J. Jung, C.B. Yun, B.F. Jr. Spencer and J.W. Seo, "Structural health monitoring of a cable-stayed bridge using smart sensor technology: data analyses," *Smart Structures and Systems*, vol. 6, no. 4-5, pp. 439-459, March. 2010
- [5] S. N. Pakzed, G. L. Fenves, S. Kim and D. E. Culer, "Design and implementation of scalable wireless sensor network for structural monitoring", *Journal of Infrastructure Systems*, vol. 14, no. 1, pp. 89-101, March. 2008
- [6] H.J. Jung, J. Park and I.H. Kim, "An energy harvesting system using wind-induced vibration of a stay cable for powering a wireless sensor node", *Smart Materials and Systems*, vol. 20, no. 7, pp.1-9, July. 2011
- [7] H. Kulah, K. Najafi, "Energy scavenging from low-frequency vibrations by using frequency up-conversion for wireless sensor applications", *IEEE Sensors Journal*, vol. 8, no. 3, pp. 261-268, March. 2008
- [8] C.R.Saha, T.O'Donnell, N.Wang and P.McCloskey, "Electromagnetic generator for harvesting energy from human motion", *Sensors and Actuators A: Physical*, vol. 147, no. 1, pp. 248-253, Sep. 2008
- [9] A. Kurs, A. Karalis, R. Moffatt, J.D. Joannopoulos, P. Fisher and M. Soljagic, "Wireless power transfer via strongly coupled magnetic resonances", *Science*, vol.317, no. 5834, pp. 83-86, Jul. 2007
- [10] J. Sallan, J.L.Villa, A.Lombart and J.F.Sanz, "Optimal Design of ICPT Systems Applied to Electric Vehicle Battery Charge", *IEEE Transactions on Industrial Electronics*, vol. 56, no. 6, pp. 2140-2148, Jun. 2009
- [11] Z.N. Low, R. A. Chinga, R. Tseng and J. Lin, "Design and test of a high-power high-efficiency loosely coupled planar wireless power

- transfer system", IEEE Transactions on Industrial Electronics, vol. 56, no 5, pp. 1801-1812, May. 2009
- [12] A. Kurs, R. Moffatt and M. Soljacic, "Simultaneous mid-range power transfer to multiple devices", Applied Physics Letters, vol. 96, 044102, Jan. 2010
- [13] J. Kim, H.C. Son, K.H. Kim and Y.J. Park, "Efficiency analysis of magnetic resonance wireless power transfer with intermediate resonant coil", IEEE Antennas and Wireless Propagation Letters, vol. 10, pp. 3898-392, May. 2011
- [14] J.M. Kim, M.S. Han and H. Sohn, "Wireless power transmission through concrete", in Proceedings of 10th International Workshop on Advanced Smart Materials and Smart Structures Technology (ANCRiSST-2014), Taipei, pp. 65-66, 2013
- [15] O. Jonah and S.V.Georgakopoulos, "Wireless power transmission through concrete via strongly coupled magnetic resonance", IEEE Transactions on Antennas and Propagation, vol. 61, no. 3, pp. 1378-1384, March. 2013
- [16] S. Cheon, Y.H. Kim, S.Y. Kang, M.L. Lee, J.M. Lee and T. Zyung, "Circuit-model-based analysis of a wireless energy-transfer system via coupled magnetic resonances", IEEE Transactions on Industrial Electronics, vol. 58, no. 7, pp. 2906-2914, July 2011
- [17] H. Hoang and F. Bien, Maximizing Efficiency of Electromagnetic Resonance Wireless Power Transmission Systems with Adaptive Circuits, Wireless Power Transfer – Principles and Engineering Explorations, InTech, 2012
- [18] U.M. Jow and M. Ghovanloo, "Design and Optimization of Printed Spiral Coils for Efficient Transcutaneous Inductive Power Transmission", IEEE Transactions on Biomedical Circuits and Systems, vol. 1, no. 3, pp. 193-202, Sep. 2007

# Simulation of ionizer module through device modelling

Younghee Kim\*, Hong-Zhou Jin\*, Panbong Ha\*, and Seungyub Park\*

Department of Electronic Engineering, Changwon National University  
Changwon 641-773, Republic of Korea  
Email: psy@changwon.ac.kr

**Abstract**—In this paper, SPICE simulation of an ionizer module generating anions is performed by using a SPICE model through curve fitting of power MOSFETs and diodes used in high voltage circuits. At the VDDH voltage of 12V, the SPICE simulation results show that HV- and HV+ voltages are -4.16kV and 3.51kV, respectively.

**Keywords**—Anion, Device Modelling, ionizer, High-Voltage, Transformer

## I. INTRODUCTION

People spend 80 ~ 90% of time indoors, and the indoor environment has an important influence on human health and work efficiency[1][2]. Anion improves the indoor air quality by removing suspended solids, eliminating odors, and reducing VOC, and also has the effect of relaxing human mood and reducing stress[3-5].

As shown in Fig. 1, the block diagram of an ionizer module circuit that generates anions using a winding-type transformer is shown in Fig. 1. This consists of a power source of VDDH(=12V), a function generator section, a semiconductor switching device, a capacitor C, a winding-type transformer, a clamping circuit, and an ion generating element[6]. The gate drive signal periodically turns on/off the power MOSFET device to generate counter electromotive force on the primary side of the transformer. The transformer boosts the counter-electromotive force voltage by the turns ratio. The high voltage of HV+/HV- is output by the clamping and rectifying circuit[7]. Ionizer used in the air cleaner generates positive or negative ions by field emission by applying high voltages of about 3.5kV/-4kV to HV+/HV-, which are carbon fiber brush discharge electrodes[6].

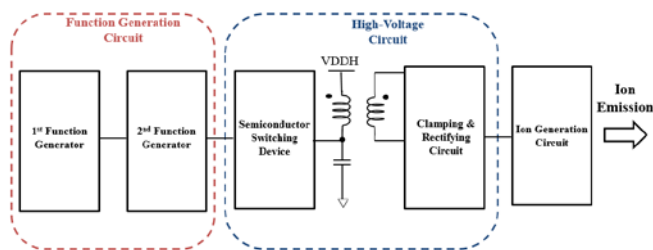


Figure 1. Block diagram of ionizer module using the winding-type transformer.

On the other hand, there is a limitation in understanding the operation principle of the ionizer module circuit and optimizing the device constants. Therefore, in this paper, we simulate a high-voltage circuit by modelling a power MOSFET and diode used in a high-voltage circuit by curve fitting.

## II. SIMULATION OF A HIGH-VOLTAGE CIRCUIT

The circuit in Fig. 2 shows the high-voltage circuit of the ionizer module. On the primary side of the transformer, an NMOS device is connected between P\_OUT and VSS. And the turn numbers of the winding-type transformer, N1 and N2, are 30 and 2600, respectively. The secondary side of the transformer is composed of diodes (HD1, HD2, HD3), capacitors (C1 and C2) and a resistor (HR1). The high voltage of HV- (= -3.5kV) and HV+ (= +4kV) are generated by the clamping and rectifying circuit.

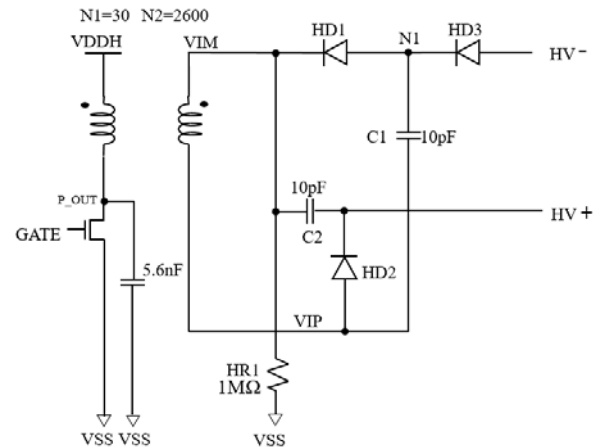


Figure 2. High-voltage circuit of an anionizer module.

To simulate the high voltage circuit, power NMOS transistor and diode are modeled by SPICE model through curve fitting. Fig. 3 (a) shows the  $I_{DS}$  curve by DC-sweeping the  $V_{DS}$  voltage while changing the gate-source voltage( $V_{GS}$ ) voltage to 3V, 5V, and 10V. This is fitted to the  $I_{DS}$ - $V_{DS}$  curve in the power NMOS specification to some extent. Fig. 3(b) shows the extraction of model parameters by curve fitting the diodes used at 25°C and 100°C.

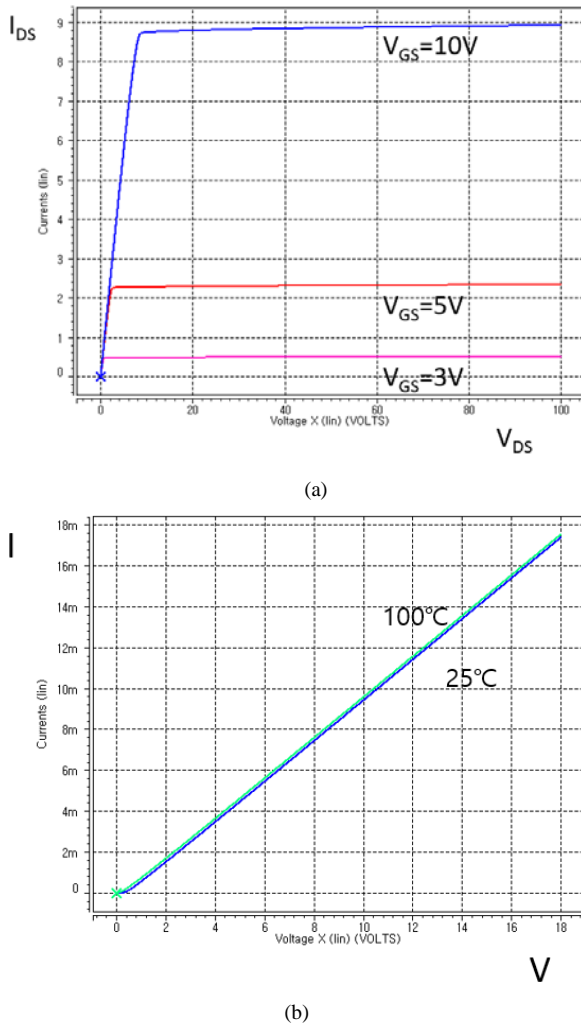


Figure 3. Device modelling for SPICE simulation (a) power NMOS and (b) diode.

Fig. 4 shows the result of SPICE simulation by modelling power NMOS, diode and transformer at 12V VDDH voltage. While the GATE signal in Fig. 2 is high, the NMOS device is turned on and energy is stored in the primary winding of the transformer. If the GATE signal is switched from high to low, counter-electromotive force is generated in the primary winding, and the P\_OUT node voltage instantaneously rises to 73V. This counter-electromotive force voltage is boosted by the transformer's winding ratio and then delivered to the secondary side. Since a resistance of  $1M\Omega$  is connected to the VIM node and VSS (Virtual ground) node, VIM drops to -75V when P\_OUT back electromotive force occurs, and VIP voltage switches from -652V to +3.39KV. At this time, it is confirmed that HV- and HV+ voltages are -4.16kV and 3.51kV, respectively.

### III. CONCLUSION

Anion improves the indoor air quality through adsorption and removal of suspended solids, elimination of odor, and reduction of VOC, and also has the effect of comforting humans and reducing stress.

In this paper, SPICE simulation of an ionizer module generating anions is performed by using a SPICE model through curve fitting of power MOSFETs and diodes used in high voltage circuits. At the VDDH voltage of 12V, the SPICE simulation result show that HV- and HV+ voltages are -4.16kV and 3.51kV, respectively.

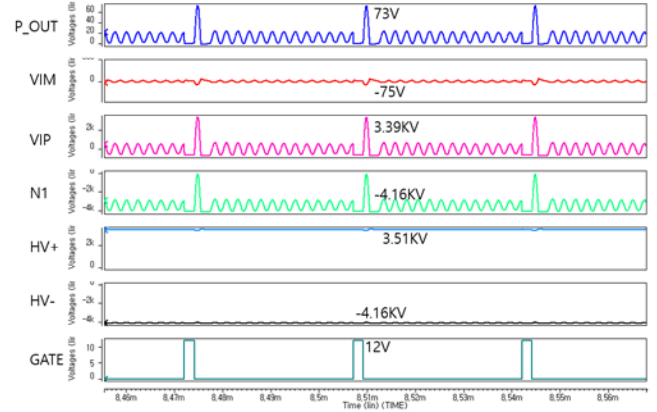


Figure 4. The result of SPICE simulation by modelling power NMOS, diode and transformer at 12V VDDH voltage.

### REFERENCES

- [1] A. P. Jones, "Indoor air quality and health", *Atmospheric Environment*, vol. 33, Issue 28, pp. 4535-4564, December 1999.
- [2] B. F. Yu, Z. B. Hu, M. Liu, H. L. Yang, Q. X. Kong and Y. H. Liu, "Review of research on air-conditioning systems and indoor air quality control for human health", *International J. of Refrigeration*, vol. 32, Issue 1, pp. 3-20, January 2009..
- [3] H Nakane, "Stress-reduction effect of negative air ions on physiological" *R&D Review of Toyota CRDL*, vol. 38. No. 2. 2003.
- [4] Munhwan Kim, "Design of a MOSFET gate driver for anion generators" MS Dissertation Thesis, Dep. of Electronic Engineering, Changwon National University, June 2017.
- [5] Sangmun Shin, "Study on the smart ionizer using dielectric barrier discharge," PhD. Dissertation Thesis, Dep. of Electrical Eng, Ulsan University, December 2013.
- [6] Younghee Kim, "Solving difficulties of ionizer products using high voltage" Planning of Solving Difficulties to Support Customized Technology Partners, Ministry of SMEs and Startups, May 2018.
- [7] Mincheol Sung et al, "Measurement of a gate driver chip for an anion generator," *KIIECT Spring Conference*, vol. 11, no. 1, pp. 116-117, May 2018.



# Development of Analog and Digital Integrated Mixer

Kwan-Woong Kim

Thunder Technology, Director in Digital Signal Processing  
Team, ChonJu, Korea

Byun-Gon Kim

Department of Electronic Engineering, Kunsan National  
University, Gunsan, Korea

Yong-Kab Kim, Juh-Yeong Suh

Department of Information and Communication  
Engineering, Wonkwang University, Iksan, Korea

Seong-Moo Yoo

Electrical & Computer Engineering, The University of  
Alabama in Huntsville, Huntsville, AL, USA

**Abstract**—Recent advances in IT technology have led to the development of innovative products incorporating IT technology in public addressing systems. In this paper, we developed an integrated mixer controller for digital public address broadcasting. We developed an integrated mixer controller that integrates the functions of a digital mixer and the controller constitutes a conventional digital public address. The integrated mixer controller has a multi-channel mixer function with 16 audio input channels and eight output channels, an EQ, matrix, and limiter for processing digital audio signals. It controls the operation status of the mixer and controls the entire public addressing system. It has internet connection function.

**Keywords**—Digital audio; DSP; AD/DA converter;

## I. INTRODUCTION

Public address broadcasting means internal broadcasting such as schools, government offices, large buildings, ports, airports, etc., and it is used for emergency broadcasting in case of an emergency such as a fire announcement as well as an on-site announcement. These conventional public address systems can be divided into analog and digital formats. Currently, many public address systems have to connect analogue base stations and broadcasting areas with several lines. When transmitting sound to a long distance, there are problems such as noise inflow and deterioration of sound quality. However, the digital public address system is superior to the analog public address system by transmitting the analog audio signal to the digital system. Therefore, the digital public address system can provide a variety of additional services such as a function of setting a sound source or background music through a PC and a network connection can be provided [1].

The core equipment of multi-channel broadcasting is a multi-channel digital audio mixer capable of input of more than 16 channels and output of more than eight channels. The multichannel digital audio mixer is implemented by applying digital audio processing technology to switch and route input and output channels, adjust channel gain, mute, equalize, band filter, and compressor/limiter functions. Therefore, the technology is changing from analog broadcasting system to digital broadcasting system. The main reason is that the development of digital audio processing technology has

enabled digital audio equipment to provide higher quality in terms of signal-to-noise ratio and signal distortion than analog. In addition, audio systems with digital audio processors can easily handle digital signals through software. Because of these advantages, programmable digital audio processors play an important role in implementing digital audio signal processing functions such as audio signal filtering, equalization, and dynamic range compression [1-7].

In this paper, we developed an integrated mixer controller for digital public address broadcasting. The integrated mixer controller has a multi-channel digital mixer for processing various sound sources, a controller function and a network interface to control BGM (background music), general broadcasting, emergency broadcasting and broadcasting system as a whole.

## II. DEVELOPMENT OF INTEGRATED MIXER CONTROLLER

The integrated mixer controller for multichannel broadcasting has 16 analog inputs, eight analog outputs and a gigabit Ethernet switching hub for communication. It has digital contact input and contact output for emergency signal reception and device control, and RS232C and RS485 communication port for serial communication. Digital audio mixers are monitored and controlled in PC-based software over the Internet.

Table 1 shows the developed integrated digital mixer controller hardware specifications.

### A. Concept and structure of hybrid mixer

Figure 1 shows an integrated mixer controller system hardware block diagram. The main components are 24-bit/96 kHz audio DSP, 32-bit embedded processor, codec, and Ethernet physical layer. The main function of the DSP is to digitize the analog signal inputted through the codec and apply the digital audio algorithm to output the processed digital signal to the codec in order to obtain high quality analog output.

TABLE I. DIGITAL MIXER CONTROLLER BLOCK DIAGRAM

Item	Specifications	
Number of audio input and output channels	Number of input channels	16
	Number of output channels	8
Audio DSP	24bit 96KHz	
Audio DSP function	<ul style="list-style-type: none"> <li>- Input volume control (-60dB ~ 10dB)</li> <li>- Input channel bass cancellation (80Hz high pass filter)</li> <li>- Input channel mute function</li> <li>- Matrix control by input channel</li> <li>- 3-band parametric EQ per input channel</li> <li>- Output channel adjustment (-60dB ~ 10dB)</li> <li>- Output channel mute function</li> <li>- Limiter function for overload protection of output channel</li> </ul>	
Processor	32 bit embedded processor	
Network interface	4 port 1 Gigabit Ethernet, 1 x RS232C 1x RS485	
Digital inputs	8 port wet/dry contact	
Digital outputs	2 port contact output	

It also has a 4-port gigabit Ethernet hub to provide network services to digital public address devices. It provides eight ports of dry/wet digital contact signal to receive emergency signal or fire signal, and provides two ports contact output for power supply and power amplifier control. The contact output is automatically output when there is an audio output signal. Figure 2 shows a real-life DSP prototype image. Figure 3 and 4 show four-channel audio input board and four-channel audio output board for audio input and output, respectively.

The microprocessor adjusts parameters such as the volume size of the DSP digital audio processor, the cutoff frequency of the crossover, and provides interaction with the user through Ethernet connections and serial communications. The network-based digital crossover provides two analog inputs and four analog outputs.

### B. System software

The DSP mixer software block of the integrated mixer controller consists of various components as follows. 1) 3-band parametric EQ, 2) 80Hz high pass filter, 3) 16 × 16 matrix, 4) I/O volume control and 5) output limiter. The basic filter for EQ is a bi-quad IIR filter. Figure 5 and equation (1) are the block diagram and differential equation of the bi-quad IIR filter. The output ( $y[n]$ ) of the filter is determined by the current input ( $x[n]$ ) and the previous input ( $x[n-1]$ ) and the previous output ( $y[n-1]$ ). For this reason, the IIR filter is called a recursive filter, and the characteristics of the filter are determined by the input coefficient ( $b_0, b_1, b_2$ ) and the feedback factor ( $a_1, a_2$ ).

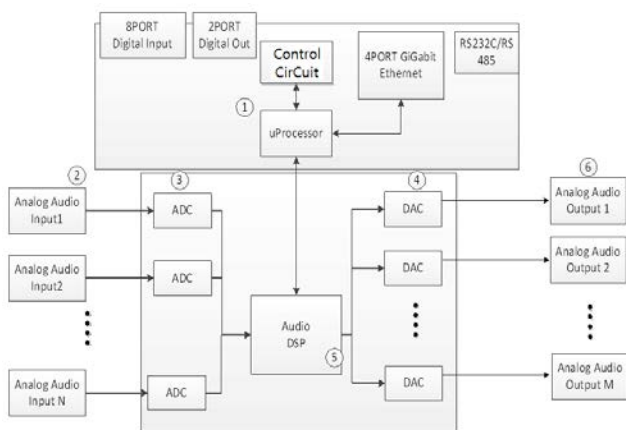


Figure 1. Structure of hybrid mixer

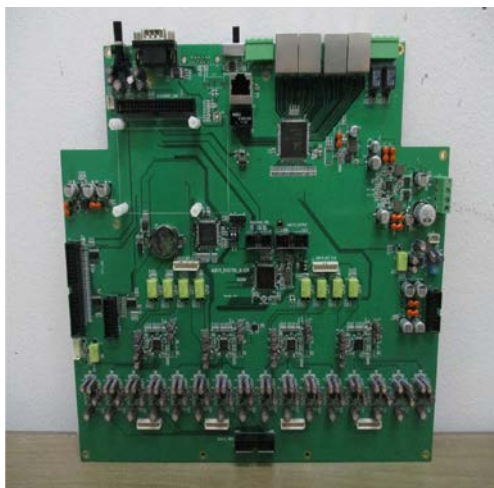


Figure 2. Prototype of integrated mixer controller

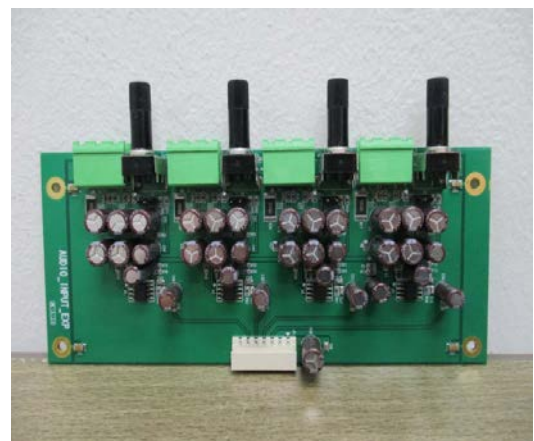


Figure 3. Structure of hybrid mixer

The crossover filter consists of 2~4 bi-quads as shown in Figure 5 and can implement Linkwitz-Riley, Butterworth and Bessel filter, and provides 12 dB/oct ~ 48 dB/oct. The embedded processor firmware performs the function of calculating the coefficient of the DSP processor by calculating the filter coefficient ( $a_1 \sim b_2$ ). The microprocessor firmware also calculates and sets digital DSP crossover algorithm parameters such as gain level, crossover cutoff frequency, crossover type, and Q, frequency, and boost values for each

band of EQ. All setting parameters are executed by the GUI control program as shown in Figure 7. The integrated mixer controller software runs on a Linux real-time OS and is developed using the GNU C ++ compiler. Figure 6 shows the block diagram of the embedded processor.

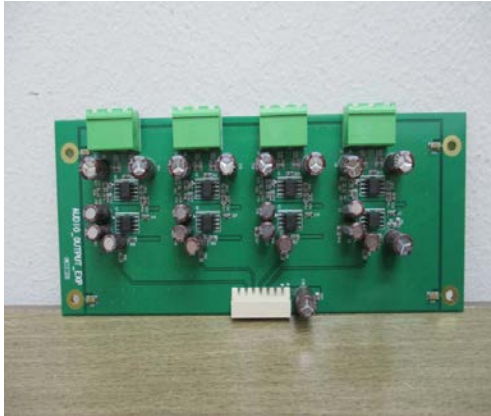


Figure 4. Prototype of integrated mixer controller

$$y[n] = \sum_{i=1}^2 (-a_i y[n-i]) + \sum_{i=0}^2 (b_i x[n-i]) \quad (1)$$

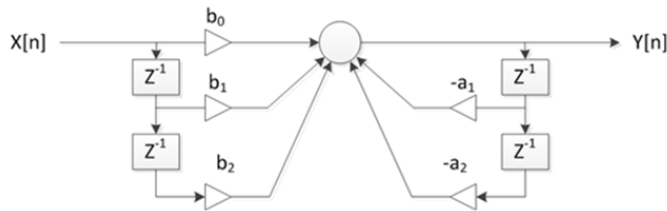


Figure 5. Bi-quad IIR filter

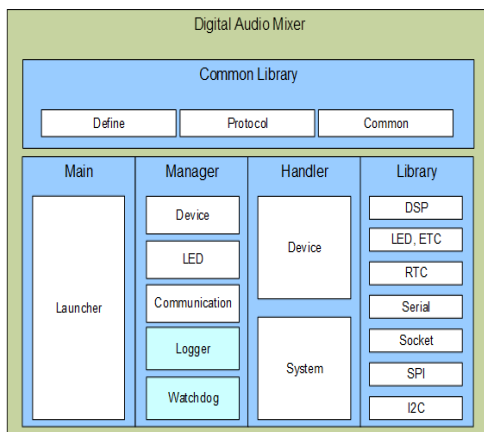


Figure 6. Software block diagram

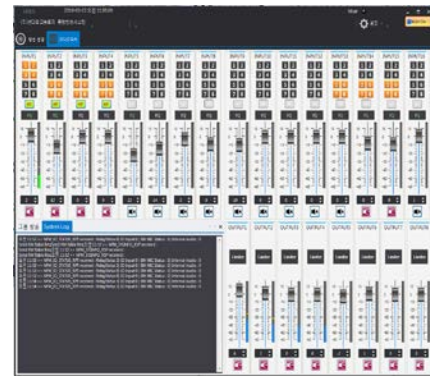


Figure 7. MixerController Main UI

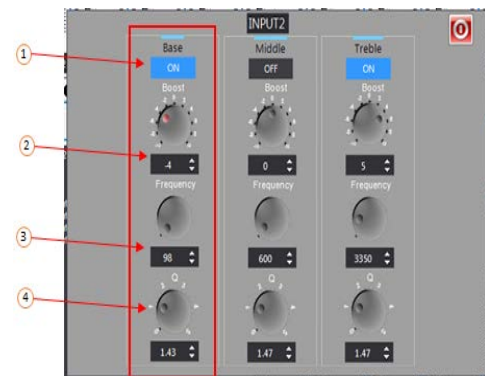


Figure 8. EQ configuration UI

The software source structure consists of a Launcher that executes Main, a Device Manager that manages each device, an LED Manager that manages LEDs, a Communication Manager that manages UI and communication, a Logger that records operation logs, a Watchdog that manages each process, Device Handler to run each device, System Handler to support system related operation, DSP Library with DSP related functions, LED Library with LED and other functions, RTC Library with RTC related functions, RS232, RS485 serial Library with functions, Socket Library with Communication related functions, SPI Library, and I2C Library.

The GUI control program was developed as a window-based software and performs sound parameter setting and status monitoring functions of the developed DSP board. Main functions include control of all functions of DSP such as volume control, EQ setting matrix control, audio signal mixing, compressor/limiter setting through network. Device search and device register function for device control, time setting function for time control, and zone setting function to send out evacuation broadcast when fire signal is received. Figure 7 and 8 show the UI of the developed operating program.

### III. PERFORMANCE TEST

The audio performance of the implemented integrated mixer controller is measured with parameters such as frequency response, signal-to-noise ratio and distortion factor. The main performance indicators of the audio processor are frequency response, distortion (THD + N), and S/N ratio. To evaluate the performance of the developed DSP board, performance was measured using AP audio analyzer.

TABLE II. TEST TYPE

Turn	Item	Measuring range
1	Frequency response	20 ~ 20,000Hz $\pm 3$ dB
2	Signal-to-noise ratio	0 ~ -140dB
3	THD + N	0 ~ 100 %

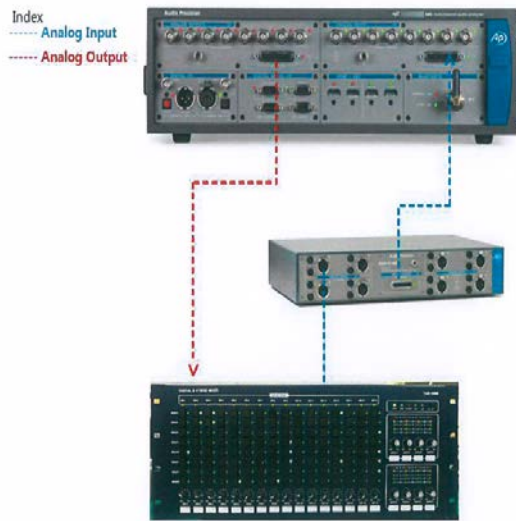


Figure 9. Audio test configuration

The frequency response characteristic of the integrated mixer controller shows almost linear characteristics in the frequency range of 20 to 20k Hz as shown in Figure 10. The distortion factor (THD + N) shows good performance below 0.02% in the audio frequency band as shown in Figure 12. As shown in Figure 11, the S/N ratio is below -90dB. This performance is better than the analog system noise.

Therefore, it can be confirmed that the performance of the implemented integrated mixer controller satisfies the sound quality performance of digital public address broadcasting in phase response, crosstalk, frequency versus signal/noise characteristics as shown in Figure 10-12.

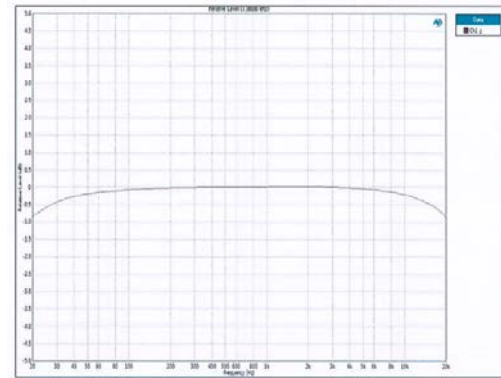


Figure 10. Frequency response

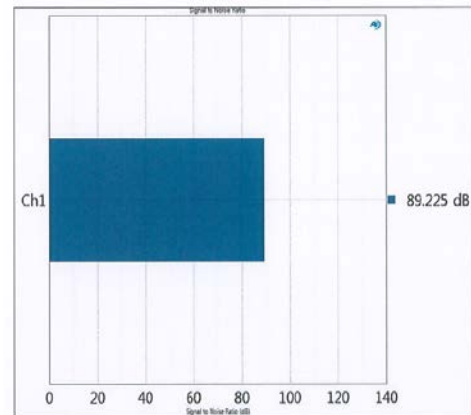


Figure 11. Signal-to-noise performance

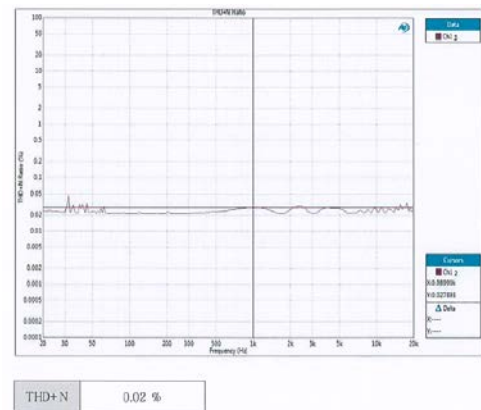


Figure 12. Signal-to-noise performance



#### IV. CONCLUSION

Digital signal processing technology is an essential technology for developing professional audio devices. The use of network-based digital signal processing technology is cost-effective, easy to maintain, can reduce analog interference, and can be developed quickly. In this paper, we developed an integrated mixer controller for digital public address broadcasting. The integrated mixer controller has a multi-channel digital mixer for processing various sound sources, a controller function and a network interface to control BGM, general broadcasting, emergency broadcasting and broadcasting system as a whole. The controller provides remote monitoring and remote control via the Internet connection. Performance tests of the developed integrated mixer controller can provide audio quality to meet the requirements of the digital public address market.

#### REFERENCES

- [1] Jung-Sook Kim and Chee-Won Song "Development of Integrated Public Address System for Intelligent Building," *Journal of The Korean Institute of Intelligent Systems*, vol. 21 no. 2, pp. 212-217, 2011.
- [2] Milan Uskokovif, Bojan IvanEevif, "The implementation of digital audio processors in analog multimedia audio systems" , *ICEcom 2003*, pp. 131-134, Duboronik, Croatia, 1 - 3 October 2003.
- [3] H. R. Jang, S. H. Kim, and Y. H. Chang, "A digital signal processor for low power," in *Proc. AP-ASIC*, pp. 42-45, 1999.
- [4] J. Nurmi, V. Eerola, E. Ofner, A. Gierlinger, I. Jemej, T. Karema, and T. Raita-aho, "A DSP core for speech coding applications," in *Proc. ICASSP*, vol. 2, pp. 429-432, 1994.
- [5] J. Eyre and J. Bier, "The evolution of DSP processor: from early architectures to the latest developments," *IEEE Signal Processing Magazine*, March 2000.
- [6] M. Dolle, S. Jhand, W. Lehner, O. Muller, and M. Schlett, "A 32-bit DSP microprocessor with reduced complexity," *IEEE J Solid-State Circuits*, vol. 32, pp.1056-1066, Jul. 1997.
- [7] Chai-Bong Lee and Chang-Young Lee, "Radiational characteristics of speaker directivity using active control," *The Journal of the Korea Institute of Electronic Communication Sciences*, Vol. 1 no. 1, pp. 27-31, 2012.
- [8] Oh-Sang Kwon, "A New Adaptive Controller Compensating Nonlinear Distortions of a Speaker," *The Journal of the Korea Institute of Electronic Communication Sciences*, Vol. 9 no. 10, pp. 1087-1094, 2012.

# A Study on the Implementation of Big Data for Suicide Prevention Programs

Hye-Jung Chang

School of Integrated Tech. & Entrepreneurship  
ChungWoon University  
HongSeong, Korea  
mschang@chungwoon.ac.kr

**Abstract** - In a rapidly changing environment, big data is becoming important as a response capability through rapid situational awareness. The human desire for safety related to human life is a basic need. The purpose of this study is to propose a suicide prevention safety program that responds to the latest increase in suicides through big data collection and analysis. To this end, we will study the process of creating a pool of big data, selecting data items that discover suicide syndrome, and developing suicide prevention programs.

**Keywords-component;** *Big data , Data classification, Suicide Prevention, Safety Data Analysis, Safety Data Pool , WHO Safety community*

## I. INTRODUCTION

Human desire for safety is a fundamental need for life, and humans can move from the next stage in which they need to fulfill their basic needs to be quickly changed [1]. Situational awareness is an area associated with human cognitive activities, and is an effective means of decision making by expressing vast amounts of data in a limited space for human cognitive expansion purposes [2]. In a society where change is rapid, in terms of time, speed is important, and rapid decision making determines the outcome's success [3].

The suicide rate in Korea has nearly tripled in the last 20 years. According to the National Statistical Office, the number of suicides per 100,000 people rose from 9.4 in 1993 to 22.6 in 2003 and 28.1 in 2012. It is the top OECD member country. As Figure 1 shows, suicide can be prevented by social efforts,

As shown in Finland, where the suicide rate has been reduced by half after 30 years of national effort. Therefore, it is necessary to carefully evaluate the effectiveness of the government support policy in accordance with the life cycle of childbirth, which leads to marriage, pregnancy, and childcare, and to devise measures to provide more tangible support from a consumer perspective. There is a lack of a systematic system for the seriousness of the situation.

The WHO Safety Community has implemented the city of safety through its major projects to prevent damage and anxiety, create a safe living environment, and improve and maintain safety [4].

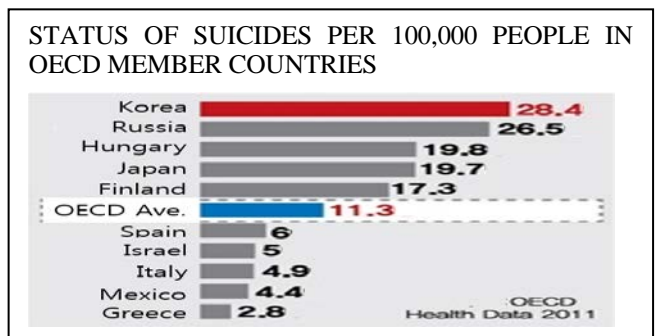


Figure 1. Status of suicides per 100,000 people in OECD member countries

In this study, the WHO safety city model's 'scientific approach to damage' is used as a frame for the basic analysis as shown in Figure 2[4].

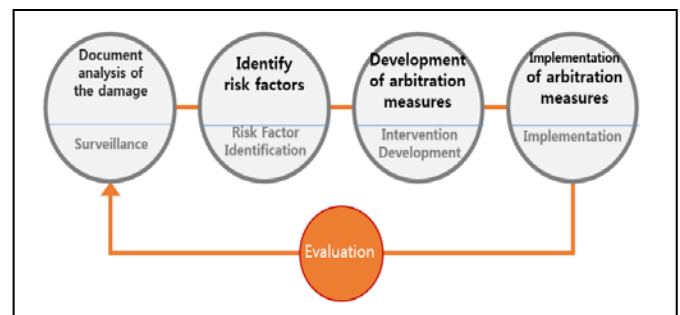


Figure 2. Big Data Analysis framework

## II. BIG DATA TO PREVENT SUICIDE

### A. Big data pool deployment and classification criteria

Data used in the big data pool can be categorized into structured and unstructured data. As Table 1 shows, overview of city, disaster, situation of injuries, injury details are structured data, whereas injury factor can utilize either unstructured or structured data [1].

TABLE I. CLASSIFICATION AND PERSONALITY OF DATA ITEMS

Level 1 category	Data classification
overview of city	Structured data
disaster	
Situations of injuries	
Injury details	
Injury Factor	Structures / Unstructured Data

### B. Defining Big Data to Prevent Suicide

The purpose of this study is to implement suicide prevention programs through the collection and analysis of Big Data. In other words, they want to define the data needed to plan the suicide prevention program and present the analysis process.

To set up a suicide prevention program, first, the high-risk group is derived, second, the priority control target is derived, and finally the detailed program is implemented.

As Figure 3 shows, utilization data for focus target elicitation are derived from damage general status data. This means that causes and ranks of deaths (including diseases) by age, trends in deaths due to external factors (damage), and the number of suicides (per 100,000 people) per person can be found.

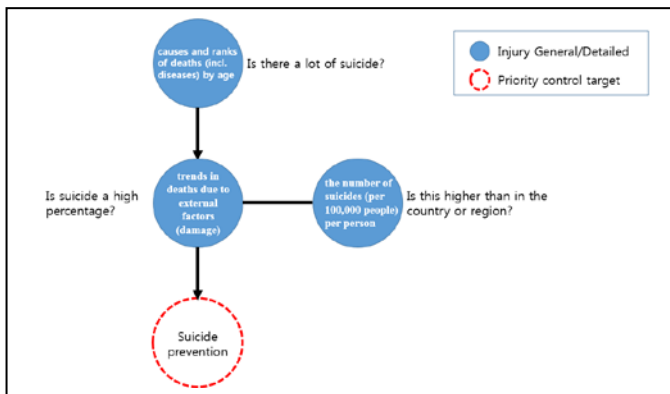


Figure 3. Priority control target Delevation Process (Death)

### C. Program elicitation process by Priority control target

Detailed data are used and analyzed as shown in Table 2 to prepare specific programs for the prevention of suicide derived as a focus target.

- Use and analyze the following data to prepare specific programs for the prevention of suicide as a focus point.
- The data on the 'Age by Age / Gender suicide death toll and mortality' identify the sex ratio at which suicide occurs (Male / Female).
- Identify which of these age groups are most likely to occur. It also checks if the suicide rate is high when

compared to countries or regions with the data of the number of suicide deaths by population age.

TABLE II. DEVELOPING SUICIDE PREVENTION PROGRAMS

Program	Utilization data	
	Level 1 Classification	Data items
Identifying the Consciousness of the Elderly	Injury General	Age / gender suicide death toll and mortality rate
	Injury General	Suicide fatalities by age versus population
	Injury Factor	An unresolved problem in the suicide of an aged man
Support for suicide prevention	Injury Factor	A suicide attempt
Expansion of counseling facilities	Injury Factor	Identification problem counseling status
	Injury Factor	Counseling target
Gate keeper Training	Injury Factor	Counselor response status

### D. Selection of suicide prevention program

- If the cause of suicide for a man or woman of a certain age can't be identified, it is recognized as a problem and a suicide prevention program is chosen to identify the consciousness of the age zone involved
- Set up a program to support those who have attempted suicide, reflecting the result that those who have attempted suicide are likely to attempt it again.
- The medical institution implements a suicide prevention program to check whether a medical institution or public institution is consulted, and to expand the counseling agency in case of problems.
- If there is a target for consultation, check the results of the counselor's response.
- If the data show that the person in question is not responding to suicide counseling, the role of the person in the neighborhood is important. Based on this result, the gate keeper is selected as a suicide prevention program.
- 

### E. The importance of data mapping

It is important to collect data, particularly on the injury Details and Injury Factor, when organizing suicide prevention safety programs from a big-data perspective. Because the data links define specific tasks. That is, after identifying the link between big data items and them, they should develop suicide prevention programs [5][6].

If coordination data is lacking at each stage, it is difficult to clearly identify the real cause of suicide prevention because the clear link between the data is unknown. What this means is that connectivity between big data is more important than the amount of data. Of all big data, it is important to take advantage of the existing open structured data. In particular, unstructured data plays a significant role in identifying the source of damage.

For the general status of the injury and the detailed status of the injury, comprehensive use of the damage death data and damage injury data is effective.

- The data on the ' Age by Age / Gender suicide death toll and mortality ' identify the sex ratio at which suicide occurs (Male / Female).
- A wide range of damage injury data should be focused on the frequency and extent of the damage.
- The injury detail status should include a variety of data items (middle and small groups) of subjects, locations, times, behaviors and conditions, types and degrees of injury.
- Detailed injury status should provide a more specific distinction between classes and sub-separation items.
- It should contain a variety of data related to the causes of damage to the primary target, from the data on safety and anxiety felt by local residents in the region for the items of damage.

Efforts should be made to reduce the number of such occurrences with direct cause data that could cause damage.

#### F. Process for suicide prevention program

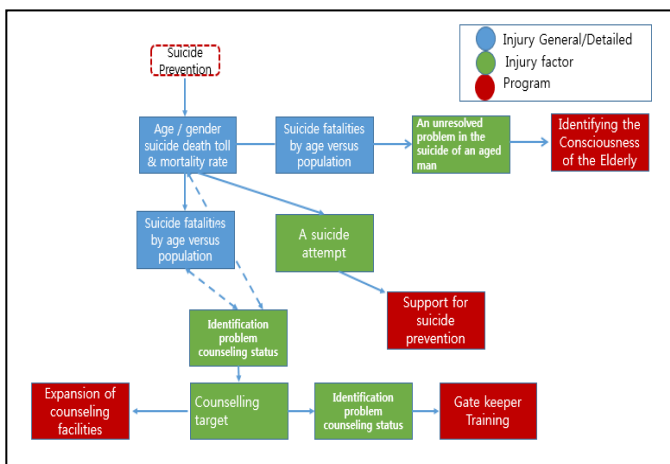


Figure 4. Big Data and suicide prevention program processes

Figure 4 shows the implementation of the suicide prevention program with big data. The data to be verified are already described in Table 2. Formatted data, injury general data and injury detailed data, can be found in regions or countries.(Blue in Figure 4).

However, it is important to use unstructured data, the data that is the cause of the injury, to determine the real cause.(Green in Figure 4).

Without the link between structured and unstructured data, it is difficult to execute accurate suicide prevention programs.

### III. CONCLUSION AND FUTHER STUDY

Rapid technological development and changes in the world can only add to the anxiety about reality, such as stress on change and loss of control.

In this paper, Korea, the country with the highest suicide rate among OECD countries, presented objective and scientific methods of preventing suicide in terms of big data to clear this stigma. Already we have structured data on the general damage of a country or region, but the association between the item and the suicide prevention program should be carefully considered.

It is also important to collect and store unstructured data at the site of the source of the damage. In order to run programs that can be applied and prevented in real life, it is important to look at unstructured data for the connectivity and root cause analysis of open structured data from a big-data perspective.

In addition, providing objective and scientific data to local residents for continuous interest and participation by the community will increase interest in suicide prevention programs.

Future studies hope to develop a program centered on the beneficiaries through design sinking methods and big data with government or local agencies implementing suicide prevention programs on site.

### REFERENCES

- [1] H.J. Chang, D.N.Kim, "A Study on the Implementation of Big Data for Child Safety Programs", The 3rd International Conference on Information, Electronics, and Communication Technology (ICIECT 2017), 2017.6
- [2] S.B. Chae, "Big Data : Industrial epicenter of catclysm," SERI, CEO Information, Vol. 85, pp. 1-22, 2012.
- [3] G.Y. Min, D.H. Jeong, "Research on Assessment of Impact of Big Data Attributes to Disaster Response Decision-Making Process", CALSEC, Vol.18 No.3, pp. 22-25, 2013.
- [4] H.J. Chang, "Implementation of the Safe Community in p.erspective of Big Data in Smart City", SungKyunKwan University doctoral thesis, 2017. 2
- [5] H.J. Chang, D.N.Kim, "A Study on inhabitants self-help scheme via sociotechnology for disaster safety of the smart city - Mainly on lessons of Kamaisi-city in Japan", JKIIECT 16-08, Vol.9 No.4 , 388-403 , 2016.8
- [6] H.J. Chang, D.N.Kim, "A Study on data utilization for implementation of the resident participation type safe community planning of the smart city", JKIIECT 16-10, Vol.9 No.5 , 478-495 , 2016.1



# Electronic vehicle on fork Device of agriculture

Lee sang-sik\*

Department of Biomedical Engineering  
Catholic Kwandong University  
Gangneung, Republic of Korea  
lsskyj@cku.ac.kr

**Abstract**— This study was started for the development of agricultural electronic vehicle by structural analysis of fork devices of agricultural electronic vehicle. Based on the solidworks, I studied the physical properties based on simulation and basic science. Structural analysis of the fork of agricultural electrical vehicle equipment should make it easier for people who are engaged in agriculture and those who operate machinery.

**Keywords** : Electronic vehicle, Fork device, Agriculture

## I. INTRODUCTION (HEADING 1)

At present, the agricultural society is in short supply due to the urbanization of young people and lack of labor and aging. In such a situation, it is more difficult to harvest harvests, especially orchards, without the aid of machines and tools. Due to the nature of agriculture, the disease of the elderly is also deepening due to repetitive movements. The existence of agricultural vehicles is very important in solving these problems. Agricultural vehicles are also used for general industrial purposes and are an indispensable element in agricultural society. For this reason, the agricultural vehicle usually uses a model equipped with a fork device, but the structure analysis of the fork device is quite long and it may be difficult to work at present. In order to solve this problem, we try to design a better agricultural work vehicle through the structural analysis of the fork device model of the agricultural vehicle.

## II. EASE OF USE

### A. Fork device 3D modeling)

First, we started 3D modeling using solidworks for a fork device for agricultural vehicles. We calculated the structure of our fork device by citing the design of existing agricultural vehicle.

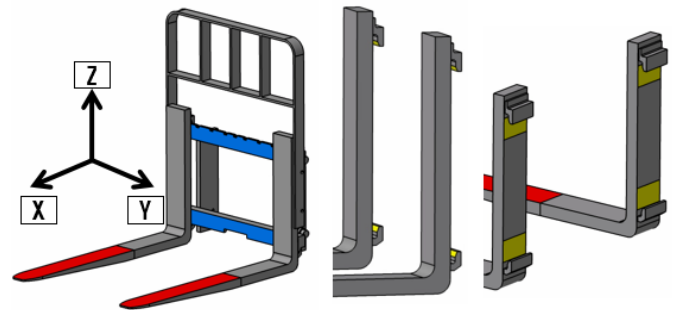
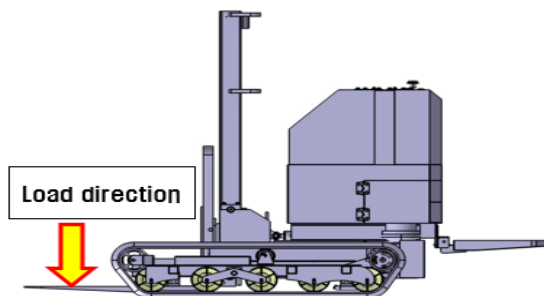


Figure 1. Completed 3D modeling and fork device structure

## III. RESULT

The condition was analyzed by applying a load of 500 kg to a fork area of 50%. The application criteria and results are as follows.

TABLE I. FIRST CONDITION AND STRUCTURE ANALYSIS OF FORK DEVICE

Application criteria	
Yield Strength	686 Mpa
Force	500 kgf
Result value	
Von-mises Stress[Max]	73.9 Mpa
conclusion Von-mises stress [maximum strain stress] was about 10.7% of the yield strength, which means safety. Reference Max. Principal Stress : 76.1 Mpa Max. Deformation : 6.9 mm	

TABLE II. SECOND CONDITION AND STRUCTURE ANALYSIS OF FORK DEVICE

Application criteria	
Yield Strength	686 Mpa
Force	500 kgf
Result value	
Von-mises Stress[Max]	63.5 Mpa

conclusion

Von-mises stress [maximum strain stress] was about 9.3% of the yield strength, which means safety.

Reference

Max. Principal Stress : 66.3 Mpa

Max. Deformation : 5.5 mm

#### IV. CONCLUSION

The present study was conducted to fork device model structural analysis of the agricultural vehicle. Structural analysis has resulted in the desired direction. Agricultural vehicles are also used in industrial applications to transport agricultural society and materials. In Korea, the number of people engaged in agriculture is gradually decreasing, and machinery elements such as agricultural vehicles are essential to supplement the reduced workforce. However, there are not many institutions and research institutes that specialize in researching and reinforcing such machine elements as agricultural vehicles. In this study, we have started to overcome these problems. The research is only for the structural analysis of the fork device, but the final goal is to develop a finished agricultural work vehicle that overcomes the problems of the current model.

#### ACKNOWLEDGMENT (HEADING 5)

The preferred

#### REFERENCES

- [1] [1] Jung Ji-Yeon, Hwang Hee-Jin, "A study on the Revitalization of the Emergency Medical Services for a Aged Society – Based on Possible Solutions to Improve Early Response System for Geriatric Emergency Patients", *Journal of Fire Science and Engineering*, Korea Institute of Fire Science and Engineering Volume 22, Issue5, 2008, pp.99-104
- [2] [2] Dabid M Demarini, Lance R Brooks, Sarah H Warren, Takahiro Kobayashi, M Ian Gulmour, Pramila Singh, "Bioassay-directed fractionation and salmonella mutagenicity of automobile and forklift diesel exhaust particles.", *Journal of Environ Health Perspectives*, 112(8), 2004, pp. 814-819.
- [3] [3] Tore J. Larsson, George Rechnitzer, "Forklift trucks-Analysis of severe and fatal occupational injuries, critical incidents and priorities for prevention", *Journal of Safety Science*, Volume 17, Issue 4, 1994, PP. 275-289.
- [4] [4] Tua Agustinus Tamba, BongHee Hong, Keum-Shik Hong, "A path following control of an unmanned autonomous forklift", *International Journal of Control, Automation and System*, Volume 7, Issue 1, 2009, pp. 113-122
- [5] [5] Tae-Hoon Kim, Seung-Jun Lee, Woojin Choi, "Design and control of the phase shift full bridge converter for the on-board battery charger of the electric forklift", *Browse Conferences 8th International Conference on Power Elctronics-ECCE Asia*, 2011
- [6] [6] Tim Horberry, Tore J Larsson, Ian Johnston, John Lambert, "Froklift safety, traffic engineering and intelligent transport system: a case study", *Journal of Applied Ergonomics*, Volume 35, Issue 6, 2004 PP. 575-581
- [7] [7] Jan-Florian Hoefinghoff, Andreas Jungk, Werner Knop, Ludger Overmeyer, "Using 3D Field Simulation for Evaluating UHF RFID Systems on Forklift Trucks", *Browse Journal & Magazines, IEEE Transactions on Antennas and Propagation*, Volume 59, Issue 2, 2011, PP. 689-691

# Ultrasonic wave development for scone cutting

Jeong Jin-hyeong

Department of Biomedical Engineering  
Catholic Kwandong University  
Gangneung, Republic of Korea  
lsskyj@cku.ac.kr

Kim Jun-tae

Department of Biomedical Engineering  
Catholic Kwandong University  
Gangneung, Republic of Korea  
lsskyj@cku.ac.kr

Choi Ahn-ryul

Department of Biomedical Engineering

Catholic Kwandong University  
Gangneung, Republic of Korea  
lsskyj@cku.ac.kr

Jo Jae-hyun

Department of Biomedical Engineering  
Catholic Kwandong University  
Gangneung, Republic of Korea  
lsskyj@cku.ac.kr

Lee Sang-sik\*

Department of Biomedical Engineering  
Catholic Kwandong University  
Gangneung, Republic of Korea  
lsskyj@cku.ac.kr

**Abstract**—This study was carried out with the idea that it would be good to perform ultrasonic module addition during the operation of the surgical laparoscopic robot. In the case of a surgical robot under development, a total of seven modules were used to reduce the operative time and the patient's burden in the laparoscopic surgery. The addition of an ultrasound module to these modules leads to a reduction in the burden on the patients who undergo the aforementioned surgery, and the prognosis of the surgery will be very positive.

**Keywords:** *Ultrasonic wave, Laparoscopic surgery, Surgical robot, Surgical module, Ultrasound diagnosis*

## I. INTRODUCTION

As medical technology develops, many medical devices are developed and developed, such as diagnostic medical devices that diagnose patients, recovery medical devices that restore patients, and surgical medical devices that cut or cut the affected part. Among them, we are developing a robotic robot that can be used for a lot of surgeries for the laparoscopic surgery with 5 major cancers in South Korea. During the development of the surgical robot, we conducted additional research with the expectation that a simple ultrasound procedure and diagnosis would help the operation. This study is a preliminary study for the ultrasonic module of laparoscopic surgical robot.

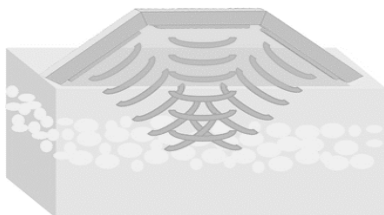


Figure 1. Estimation of Ultrasonic Energy Concentration

This material is based upon work supported by the Ministry of Trade, Industry & Energy(MOTIE, Korea) under Industrial Technology Innovation Program. No.10073055, 'Development of Module type endoscope system for single port surgery

## II. METHOD AND MATERIALS

### A. Developed high-efficiency ultrasolic oscillation circuit and control circuit

The PPL detects the phase difference of the output signal under the input signal, controls the phase of the output signal generator by the voltage proportional thereto, and makes the phase of the output signal equal to the phase of the input signal.

A phase comparator, a low-pass filter, an error amplifier, and voltage-controlled generator, It is an automatic phase control loop.

Basically, it is circuit that oscillates the VCO(Voltage controlled oscillator) at the same frequency as the input frequency. The oscillation frequency force of the VCO is given by the following equation(Fig.2.)

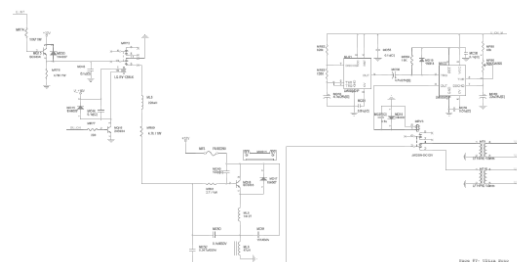


Figure 2. Plus mode generator circuit

## III. RESULTS AND DISCUSSION

The intensity of the transducer having a diameter of 10 mm at a frequency of 3 MHz takes 2.6 seconds to decompose the fat when the ultrasound is focused. Organs at risk of necrosis were about 1 minute and 20 seconds longer than fat decomposition, so no damage to organs was worried.

1) liver

$\Delta T = \frac{\alpha_{alt}}{\rho_{cm}}$  the absorption coefficient of the liver is 0.94. At 1MHz, it is applied at 3MHz, so it can be defined as  $\Delta T = 0.06^\circ \text{C}$ .

The time required to raise  $5.5^\circ \text{C}$  per second is  $5.5 / 0.06$ , which is approximately 91 seconds and 1 minute 31 seconds. That is, after a period of 1 minute and 30 seconds, necrosis of the liver occurs.

2) kidney

$\Delta T = \frac{\alpha_{alt}}{\rho_{cm}}$  the absorption coefficient of the kidney is 1. At 1MHz, it is applied at 3MHz, so it can be defined as  $\Delta T = 0.066^\circ \text{C}$ . The time required to raise  $5.5^\circ \text{C}$  per second is  $5.5 / 0.066$ , which takes about 83 seconds and 1 minute 23 seconds. That is, the time of one minute and 23 seconds is not enough to cause necrosis of the kidney.

In this study, 3MHz was the most appropriate considering the energy concentration and temperature rise rate considering the operation time.

Considering X0, it was considered efficient to select a vibrator having a diameter of 5 mm, but it was not easy to obtain a vibrator having an actual diameter of 5 mm. Therefore, a transducer array was designed using a vibrator with a diameter of 10 mm, and proper energy could be focused by adjusting the output intensity.

#### IV. CONCLUSION

In this study, 3MHz was the most appropriate considering the energy concentration and temperature rise rate considering the operation time.

Considering X0, it is considered efficient to select the oscillator of 5mm in diameter, but it was not easy to obtain the oscillator having the actual diameter of 5mm. Therefore, a transducer array was designed by using a vibrator having a diameter of 10 mm so that appropriate energy could be focused by adjusting the output intensity.

#### ACKNOWLEDGMENT (HEADING 5)

The preferred spelling of the word “acknowledgment” in America is without an “e” after the “g”. Avoid the stilted expression, “One of us (R. B. G.) thanks . . .” Instead, try “R. B. G. thanks”. Put sponsor acknowledgments in the unnumbered footnote on the first page.

#### REFERENCES

- [1] Ma J, Luo Y, Sevag Packard RR, Ma T, Ding Y, Abiri P, Tai YC, Zhou Q, Shung KK, Li R, Hsiai T, “Ultrasoni Transducer-Guided Electrochemical Impedance Spectroscopy to Assess Lipid-Laden Plaques.”, 2016, Sensors and Actuators B: Chemical, Volume 234, 154-161
- [2] Kietczewska M, Szymczyk J, Leszczynski R, Blaszczyk J, “The effect of high-frequency current ultrasonic wave on selected parameters of fat tissue.”, 2016, Polski Merkuriusz Lekarski Polish Medical Journal, Vol.8, No.239, 298-300
- [3] Rouyer J, Varray F, Pozo E, Basset O, Cachard C, Lavarello R, “Evaluation of frequency-domain ultrasonic imaging attenuation compensation technique.”, 2015, 37th Annual International Conference of the IEEE Engineering in Medicine and Biology Society(EMBC), 1560-3
- [4] D. Inbar, M. Delevy, "Time gain compensation for ultrasonic medical imaging systems", August 1 1989.
- [5] F. Varray, C. Cachard, J. Kybic, A. Novell, A. Bouakaz, O. Basset, "A multi-frequency approach to increase the native resolution of ultrasound images", Proceedings of the 20th European Signal Processing Conference (EUSIPCO), pp. 2733-2737, 2012.



# EMG response study in treadmill exercise

Lee Sang-sik

Department of Biomedical Engineering  
Catholic Kwandong University  
Gangneung, Republic of Korea  
lsskyj@cku.ac.kr

Won Jong-Chil

Department of Biomedical Engineering  
Catholic Kwandong University  
Gangneung, Republic of Korea  
lsskyj@cku.ac.kr

Choi Ahn-ryul

Department of Biomedical Engineering  
Catholic Kwandong University  
Gangneung, Republic of Korea  
lsskyj@cku.ac.kr

Lee Ki-young\*

Department of Biomedical Engineering  
Catholic Kwandong University  
Gangneung, Republic of Korea  
lsskyj@cku.ac.kr

**Abstract**—Under dynamic exercise, the muscle tension is proportional to EMG activity, and EMG indices which represent muscle activity can be classified by magnitude indices in time domain and spectrum indices in frequency domain. The purpose of this paper is to compare the activities of EMG indices during dynamic exercise, and to examine the spectrum index using spectrum moments which is better and more sensitive than traditional spectrum indices. Therefore, SM-HLR can be a high-sensitive spectrum index to reflect changes of activities of biceps femoris muscle due to walking.

**Keywords:** EMG activity, Spectrum indices, Spectrum moments, Logarithm, Treadmill walking

## I. INTRODUCTION (HEADING 1)

The activity of EMG measured during isometric or isotonic exercise is proportional to muscle strength. Therefore, it has been widely used as a method for evaluating the function of muscles from an EMG clinically, and many researchers have proposed electromyographic indices indicating muscle characteristics and information related to muscle movement and muscle relaxation so far. Have been published. In this study, we analyze the EMG using the spectrum index defined by normalizing the fifth-order spectral moment of the EMG by the (-1) -order spectrum moment, the spectral index of the EMG during the dynamic exercise, The average power frequency (MPF) and the high-bandwidth ratio (HLR). Here, the target muscle of the dynamic exercise was the biceps of the femur during treadmill walking, and the sensitivity by the variation width was compared with the change of the EMG signal due to the contraction of the biceps femoris according to the walking cycle.

## II. MATERIALS AND METHODS

### A. The arrested

The subjects of this experiment were 10 healthy adults (5 males, 5 females). Their ages ranged from 28 to 39 years

(mean 33 years), with a height of 157-180cm (mean 169.4cm) and a weight of 52-90kg (mean 70.8kg). Among these subjects, regular physical trainees, musculoskeletal and nervous system patients were excluded. The subjects who participated in the study explained the contents of the research process and signed the format document including the contents. This study was made with the permission of the Catholic University of Kwangju University Institutional Bioethics Committee.

### B. Signal processing and statistics

The EMG signals measured from the electrodes of an EMG meter(MyTace 400, Noraxon, Inc.) were amplified 1000times and stored on a PC hard disk at a 1kHz sampling frequency through a band pass filter in the range of 20-450Hz. In order to measure the EMG activity, the EMG signal was a high-low-range ratio(SM-HLR) using the RMS value, the mean power frequency(MPF), the high-to-low ratio(HLR) was extracted. The definitions of the EMG indices extracted from this study are as follows.

$$RMS = \sqrt{\frac{1}{N} \int_0^T s^2(t) dt} \quad \text{-----(1)}$$

$$MPF = \frac{\int_{f_1}^{f_2} f P(f) df}{\int_{f_1}^{f_2} P(f) df} \quad \text{-----(2)}$$

$$HLR = \frac{\int_{f_1}^{f_2} P(f) df}{\int_{f_1}^{f_2} P(f) df} \quad \text{----- (3)}$$

$$SM-HLR = \frac{\int_{f_1}^{f_2} f^5 P(f) df}{\int_{f_1}^{f_2} f^{-1} P(f) df} \quad \text{--- (4)}$$

In order to compare EMG indices, all of them were converted to logarithm [10], and the spectral exponents were normalized to 100 and then converted to a large number. To determine if the EMG signals measured twice in the experiment were statistically significant, a corresponding sample t-test was performed and the significance level was set at  $p < 0.05$ . Correlation was used to determine the similarity of EMG indices.

### III. RESULT AND DISCUSSION

The biceps femur to measure EMG signals is the muscle that works to stretch the femur, bend the knee, and turn the calves outward. In this study, the EMG index changes according to the gait cycle because it measures the contraction of the biceps femoris exercising periodically during treadmill walking. There was no significant difference between the two measured EMGs ( $p > 0.05$ ).

### ACKNOWLEDGMENT (HEADING 5)

The preferred spe

### REFERENCES

”

- [1] Brenda Bigland, O. C. J. Lippold, "Motor unit activity in the voluntary contraction of human muscle", *Journal of Physiology*, 125, pp. 322-335, 1954
- [2] De Luca, C. J., "The Use of Surface Electromyography in Biomechanics," *J. Applied Biomechanics*, Vol. 13, No. 2, pp. 135-163, 1997.
- [3] A. Phinyomark, S. Thongpanja, H. Hu, P. Phukpattaranont, C. Limsakul, The usefulness of mean and median frequencies in electromyography analysis, Computational intelligence in electromyography analysis-A perspective on current applications and future challenges, CH. 8, InTech, 2012
- [4] Lee, K.Y., Shin, K.Y., Kim, H.S., Mun, J.H., "Estimating Muscle Fatigue of the Biceps Brachii using High to Low Band Ratio in EMG during Isotonic Exercise," *International Journal of Precision Engineering and Manufacturing*, Vol. 10, No. 3, pp. 147-153, 2009
- [5] Duchene J. Goubel F., "EMG Spectral Shift as an Indicator of Fatigability in an Heterogeneous Muscle Group," *Eur. J. Appl. Physiol*, Vol. 61, pp. 81-87, 1990.
- [6] Masuda K. Masuda T. Sadoyama T. Inaki M. Katsuta S., "Changes in Surface EMG Parameters during Static and Dynamic Fatiguing Contractions," *J. Electromyography and Kinesiology*, Vol. 9, No. 1, pp. 39-46, 1999.

# A Study on the Joint Design of a Single Laparoscopic Robot

Kim Young-il

Department of Biomedical Engineering  
Catholic Kwandong University  
Gangneung, Republic of Korea  
yikstmary@gmail.com

Lee Sang-sik

Department of Biomedical Engineering  
Catholic Kwandong University  
Gangneung, Republic of Korea  
lsskyj@cku.ac.kr

Lee Woo-ram

Department of Control and Instrumentation  
Catholic Kwandong University  
Gangneung, Republic of Korea  
ramsstmary@gmail.com

Yoon Chee-soon

Department of Medical Doctor  
Catholic Kwandong University  
Gangneung, Republic of Korea  
lsskyj@cku.ac.kr

**Abstract**— The smaller the incision or ablation site during surgery, the faster the recovery. In addition, the smaller the extracorporeal incision site, the easier it is to manage and the risk of infection is reduced. Past surgery has damaged the body inefficiently, but recent surgery is directed at minimally invasive surgery. At present, minimally invasive surgery is an endoscopic surgery. Endoscopic surgery can be performed in a variety of ways, from direct surgery by a home doctor to a surgical operation through a robot. Endoscopic surgery includes cholecystectomy, colonic polypectomy, hysterectomy, and adnexectomy.

**Keywords:** Robot, Laparoscopic Robot, Joint design

## I. INTRODUCTION

The smaller the incision or ablation site during surgery, the faster the recovery. In addition, the smaller the extracorporeal incision site, the easier it is to manage and the risk of infection is reduced. Past surgery has damaged the body inefficiently, but recent surgery is directed at minimally invasive surgery. At present, minimally invasive surgery is an endoscopic surgery. Endoscopic surgery can be performed in a variety of ways, from direct surgery by a home doctor to a surgical operation through a robot. Endoscopic surgery includes cholecystectomy, colonic polypectomy, hysterectomy, and adnexectomy. A representative example of a surgical robot is the da Vinci® Surgical System (Intuitive Surgical). The robot of the da Vinci surgery has a problem that the operation in the abdominal cavity is limited because the body of the arm is long and rigid. The possibility of triangulation at the time of surgery affects the operation time and the success rate. The condition for this triangulation is that there should be at least four arms. The da Vinci robot has three arms for surgery, which is below the triangulation condition. To solve these problems, we tried to

make a robot that can operate freely within the abdominal cavity with four or more arms and multiple joints. [1-3]

In this paper, we propose an optimal forceps design that minimizes the risk of fracture by performing PE joint assembly design and PE joint strength test, which is one of the end effectors of modular surgical robots using pulleys.

## II. MAIN SUBJECT

### A. Modular surgical robot for single endoscopic surgery)

The assisting device in a state where the robot arm is coupled is inserted into the body through the main tube and coupled to the outer wall of the main tube. The main tube has an outer diameter of 20 mm and an inner diameter of 18 mm. Each module is less than 18 mm in diameter. The structure of the robot arm inserted into the main tube through the main tube connects the wire through the shaft at the bottom of the container and develops the wire inside the container and transfers it to the robot arm. The robot arm is 11 mm in diameter.

In this type of robotic arm structure, a PE string that is stronger than a steel wire must be used. The use of PE pliant to overcome the problem of difficulty in fixing the joint in the joint. It is necessary to develop joints that can fix PE braces without wire damage..

### B. Experiment of fracture strength for joint model and verification

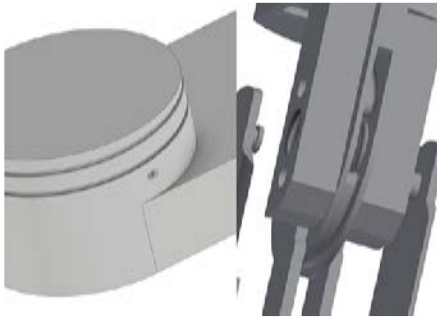
#### B.1. Joint model

There is a large difference in breaking strength depending on the bundle type of PE brace. The bundle suggests a high-rigidity model design suitable for the shape with the strongest

---

This material is based upon work supported by the Ministry of Trade, Industry & Energy(MOTIE, Korea) under Industrial Technology Innovation Program. No.10073055, 'Development of Module type endoscope system for single port surgery

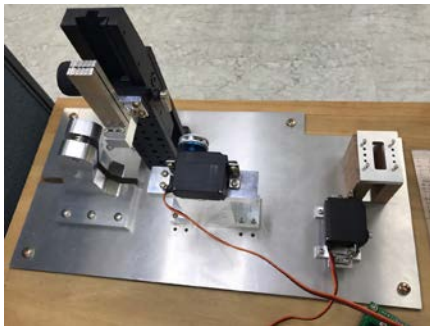
breaking strength. Fig1. shows P1 and P2 for the PR method used in the experiment.



<fig1.> Joint design (P1, P2 from top)

### B.2. Fracture strength test

The experimental apparatus consisted of controllable system, controller, and mechanism. The control system and the chuck roller are designed to perform the same operation repeatedly, and designed and manufactured so that the number of repetitions and the angle of operation can be controlled. It is designed and manufactured so that the angle of the wire can be adjusted. The experimental setup is shown in Fig2.



<fig2.> Experimental apparatus

The operation of the surgical instrument is about 1000 times, and the force required for the end is about 2N. Since the force required to operate the robot arm increases in proportion to the length of the arm, a load of 20 N, 40 N, 60 N was applied to perform 3000 times of breaking test exceeding the stable range. The test was conducted up to 3 sets of 1000 times / one set unit. The experiment was performed at the Catholic University of Korea, St. Mary's Hospital. The experiment is shown in Fig3.



<fig3.> Experiment view

### B.3. Fracture strength test

Experiments were carried out 10 times with two designs of joints as variables and the fracture strength was quantified. Table 1 shows the results of joint type fixation. From the experimental results of Table 1, it can be seen that the best result is obtained in the form of P2 which preserves the strength of the wire as it is.

Experimental results show that the fracture at the fixed part of the wire is closely related to the deformation due to the interaction between the knot and the contact surface when the tension of the wire increases.

## III. CONCLUSION

In this paper, we design and verify the joint fixation which has a great influence on the wire stability during the robot arm design process for single endoscopic surgery. The wire fracture strength test for various types of joint fixture design showed that the optimal joint fixture design minimizes the risk of fracture by applying the cover type grooves..

	20N	40N	60N
P1	88%	83%	75%
P2	98%	94%	86%

<Table1.> Experimental results by type

## ACKNOWLEDGMENT

This material is based upon work supported by the Ministry of Trade, Industry & Energy(MOTIE, Korea) under Industrial Technology Innovation Program. No.10073055, 'Development of Module type endoscope system for single port surgery

## REFERENCES

- [1] Kim Young Il, Yun Chisun, and Lee Sang Sik, "A Study on the Design of Modular Surgical Robot for Single Endoscopic Surgery", Information and Control Conference, 2017



[2] Fraud, "Surveillance colonoscopy", The Korean Journal of Gastrointestinal Endoscopy, Vol. 41, 2010

[3] Lee Kun-woo, "Single port access laparoscopic hysterectomy for large uterus of more than 500g", Korean journal of obstetrics&gynecology, Vol. 55, No. 6, pp 392-397, 2012 Unless there are six authors or more give all authors

# Efficient Two-Dimensional Antenna Group Selection Scheme for FD-MIMO Systems

Won Ho Jeong

Department of Electrical and Electronic Engineering  
Chungbuk National University  
Cheongju, Chungbuk, Rep. KOREA  
whjeong@cbnu.ac.kr

Kyung-Seok Kim

Department of Electrical and Electronic Engineering  
Chungbuk National University  
Cheongju, Chungbuk, Rep. KOREA  
kseokkim@cbnu.ac.kr

Nam-il Kim

Department of 5G Giga Communication Research  
Laboratory

Electronics and Telecommunications Research Institute  
Daejeon, Rep. KOREA  
namilk@etri.re.kr

Ju-Phil Cho

Department of Radio Communication Engineering  
Kunsan National University  
Gunsan, Rep. KOREA  
stefano@kunsan.ac.kr

Sang-Lim Ju\*

Department of Electrical and Electronic Engineering  
Chungbuk National University  
Cheongju, Chungbuk, Rep. KOREA  
\*Corresponding Author: imaward@naver.com

**Abstract**—In 5G mobile communications, radio-frequency (RF) chain and complexity reduction are very important issues, and performance improvement in these areas is required. Thus, RF chain reduction and spectral efficiency (SE) enhancement should be implemented in parallel. In this paper, an efficient antenna selection scheme is proposed for full-dimension multiple-input multiple-output (FD-MIMO) systems based on three-dimensional (3D) channels for 3D beam formation. In the proposed algorithm, virtual antenna groups are used to maintain two-dimensional antenna arrays for FD-MIMO systems. Three antenna selection schemes were used to increase the SE: norm-based selection, capacity-based reduced-complexity exhaustive searching, and 3D-norm based reduced-complexity exhaustive search. We compared the proposed antenna selection algorithm with the previously existing algorithms using the same number of antennas and confirmed that SE was improved by using the proposed algorithm, even with RF chain reduction. The proposed antenna selection algorithm provides significant improvements over the existing algorithms in terms of both SE and computational complexity.

**Keywords**—component; 5G communication; FD-MIMO; antenna selection; RF chain; spectral efficiency

## I. INTRODUCTION

New mobile communications systems require higher spectral efficiencies and data capacities. Full-dimension multiple-input multiple-output (FD-MIMO) systems are considered to be among the promising types of systems that could serve as next-generation mobile communication systems. The improved performance offered by FD-MIMO systems is achieved by adaptive transmission beam formation at evolved node B (eNB) antennas [1,2]. However, FD-MIMO systems

have hardware complexity problems because they require large numbers of antennas and, most importantly, radio-frequency (RF) chains [3]. Therefore, studies have been actively conducted with the objective of improving the system performance when a constant, large number of antennas is selected. When an antenna is selected, the number of RF chains decreases accordingly. The purpose of our study was to improve the system performance while maintaining a constant number of RF chains. Conventional antenna selection techniques in massive MIMO systems are greedy searching and vector calculation, for which representative antenna selection methods are capacity-based reduced-complexity exhaustive searching (CBRCS) and norm-based selection (NBS), respectively [2,4]. We developed an efficient two-dimensional (2D) antenna group selection scheme for vector calculation with relatively low complexity and analyzed the differences in performance between the proposed and conventional algorithms. The spectral efficiency (SE), beamforming gain, and complexity were obtained analytically and confirmed by numerical results.

The remainder of this paper is organized as follows. Section II introduces the flow of our system model. Section III explains the proposed efficient 2D antenna selection scheme. The performance simulation results and corresponding analysis are presented in Section IV, and Section V provides concluding remarks and summarizes the paper.

## II. SYSTEM MODEL

In an FD-MIMO system, adding complete RF chains typically results in increased complexity, size, and cost. These negative effects can be drastically reduced by antenna

---

This work was supported by Institute for Information & communications Technology Promotion(IITP) grant funded by the Korea government(MSIT). [No. 2016-0-00183, Development of 5G mobile access platform technology based on virtualization converged with computing]

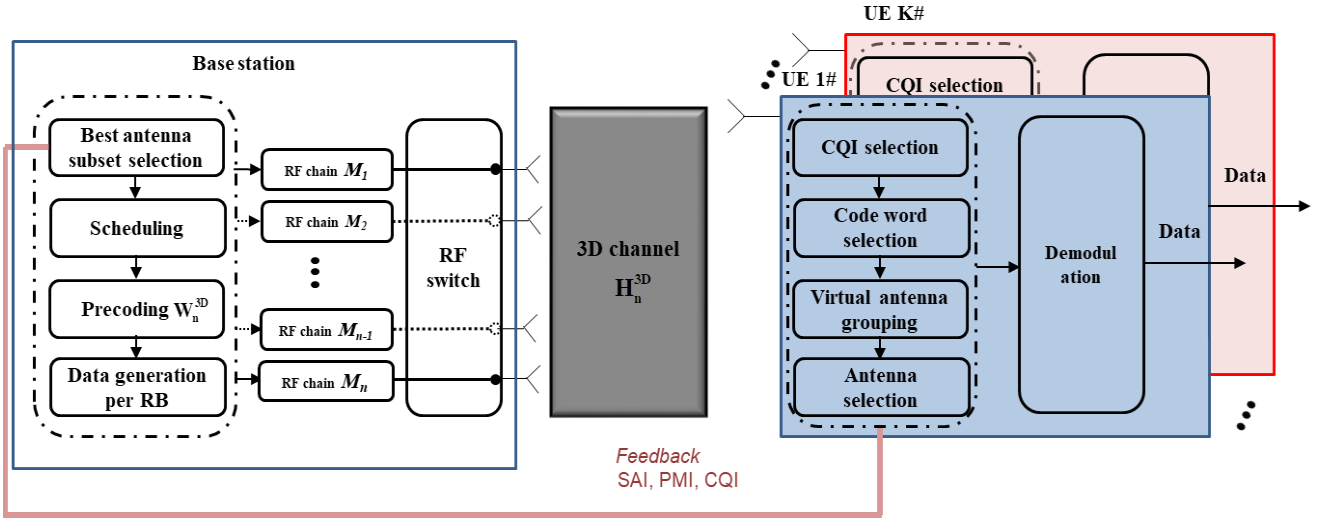


Figure 1. FD-MIMO system model for antenna selection.

selection, because antenna elements and digital signal processing are considerably cheaper than complete RF chains. In addition, many of the benefits of FD-MIMO schemes can still be obtained. In this paper, we discuss downlink FD-MIMO systems with  $N$  transmission antennas at one base station (BS) and a single receiving antenna with  $K$  users, as shown in Fig. 1. The maximum number of transmission antennas is 64, and the selected antenna number is  $L$ . To reduce RF chain  $M$ , the RF chain in the BS and the selected antenna are considered to be the same ( $L = M$ ). In multi-user FD-MIMO systems, the signals received by users can be expressed as follows:

$$y_k = \underbrace{\sqrt{P_{n,k}} H_{n,k}^{3D} W_{n,k}^{3D} x_{n,k}}_{\text{Desired signal}} + \underbrace{\sum_{i=1, i \neq k}^K \sqrt{P_{n,i}} H_{n,i}^{3D} W_{n,i}^{3D} x_{n,i}}_{\text{Interference signal}} + n_0, \quad (1)$$

where  $P$  is the transmission power of the  $N^{\text{th}}$  antenna for user  $k$ ,  $H$  is the 3GPP 3D channel,  $W$  is the precoding matrix,  $x$  is the transmitted signal, and  $n_0$  is the zero-mean Gaussian noise. The signal received by the  $k^{\text{th}}$  user from the selected best  $l^{\text{th}}$  antenna can be rewritten as

$$y_k = \underbrace{\sqrt{P_{l,k}} H_{l,k}^{3D} W_{l,k}^{3D} x_{l,k}}_{\text{Desired signal}} + \underbrace{\sum_{i=1, i \neq k}^K \sqrt{P_{l,i}} H_{l,i}^{3D} W_{l,i}^{3D} x_{l,i}}_{\text{Interference signal}} + n_0, \quad (2)$$

where  $P$  is the power transmitted by the selected  $l^{\text{th}}$  antenna for user  $k$  with the total power constraint  $\sum_{i=1}^k P_{l,i} < P$ . In this paper, equal power allocation among the scheduled users is assumed, i.e.,  $P_{l,i} = P/K$ ,  $i = 1, \dots, K$ . By defining

$$\rho_{l,k} \triangleq \frac{P}{K \sigma_{l,k}^2}, \quad (3)$$

the signal-to-interference-plus-noise ratio (SINR) for user  $k$  can be expressed as

$$\text{SINR}_k = \frac{\rho_{l,k} |H_{l,k}^{3D} W_{l,k}^{3D}|^2}{\sum_{i=1, i \neq k}^K \rho_{l,i} |H_{l,i}^{3D} W_{l,i}^{3D}|^2 + 1}, \quad (4)$$

and the achievable ergodic rate of user  $k$  is

$$R_k = \mathbb{E}[\log_2(1 + \text{SINR}_k)]. \quad (5)$$

Consequently, the sum of the ergodic rates of the system is

$$R_{\text{sum}} = \sum_{k=1}^K R_k \quad (6)$$

In this paper, it is assumed that each user terminal has perfectly accurate effective channel state information (CSI) about itself and that the BS has only the statistical CSI for each user.

### III. EFFICIENT 2D ANTENNA SELECTION SCHEME

#### A. Virtual Antenna and 3D Channel Grouping

Increasing the number of antennas improves the SE but requires highly complex 3D channels. The following describes a method of effective antenna selection in FD-MIMO systems. Specifically, we propose a transmission antenna selection scheme to enhance the existing selection schemes. Fig. 2 depicts the 2D antenna grouping procedure for a uniform planar array (UPA). The procedure for virtual antenna

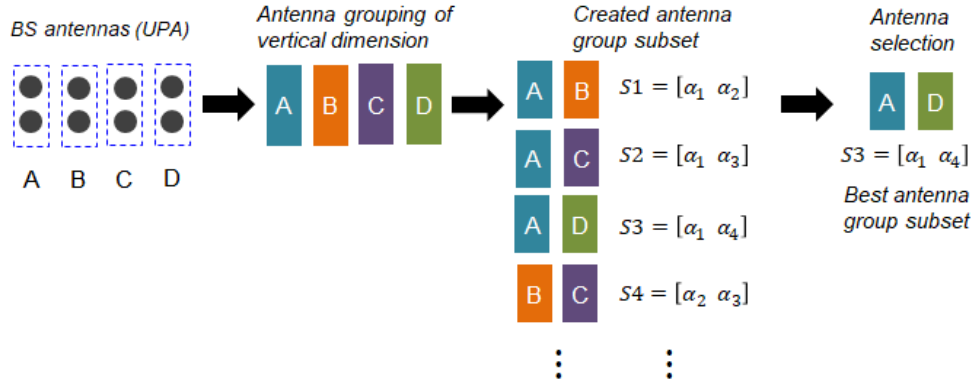


Figure 2. 2D antenna grouping procedure for a UPA.

grouping is as follows. The 2D array antenna configuration can be written as [5,6]

$$n_p = \frac{1}{\sqrt{P}} \exp\left(-j \frac{2\pi}{\lambda} (p-1)d_H\right), \quad (7)$$

$$n_q = \frac{1}{\sqrt{Q}} \exp\left(-j \frac{2\pi}{\lambda} (q-1)d_V \cos\theta_{ilt}\right), \quad (8)$$

where  $p$  and  $q$  correspond to the horizontal and vertical antenna elements, respectively. The 2D antenna array configuration is determined by the horizontal and vertical distances  $d_H$  and  $d_V$ , respectively, and can be rewritten as follows with virtual antenna group subset  $S$ :

$$S(\bar{n}_p) = \left[ \frac{\frac{1}{\sqrt{P}} \exp\left(-j \frac{2\pi}{\lambda} (p-1)d_H\right) \times \frac{1}{\sqrt{Q}} \exp\left(-j \frac{2\pi}{\lambda} (q-1)d_V \cos\theta_{ilt}\right)}{q_{num\_group}} \right] \quad (9)$$

The vertical axes are grouped by  $q_{num\_group}$ , and the channels are grouped according to the grouped antenna configuration. The procedure for 3D channel grouping is addressed next. The channel coefficients in a 3GPP 3D channel can be expressed as follows [7]. The random rays of the 3D channel coefficients are associated with the antenna field pattern. The 2D antenna array field pattern in a 3D channel is given by [6]

$$\hat{r}_{rx,n,m} = \begin{bmatrix} \sin \theta_{n,m,ZOD} \cos \phi_{n,m,AOD} \\ \sin \theta_{n,m,ZOD} \sin \phi_{n,m,AOD} \\ \cos \theta_{n,m,ZOD} \end{bmatrix}. \quad (10)$$

The virtual antenna grouping  $G$  of a 3D channel can be rewritten as follows:

$$G = \left[ \frac{\sum_{i=1}^q H_{p,i}^{3D}}{q_{num\_group}} \right]. \quad (11)$$

Again, the vertical axes of the 3D channel are grouped by  $q_{num\_group}$ . Fig. 3 shows an example of channel selection for 2D antenna grouping. The antenna selection algorithm was applied with virtual grouping of the 3D antennas and channels.

#### B. Proposed 2D Antenna Selection Scheme

The subset is constructed by calculating the norm using [8]

$$\|g(\bar{H}_{kp})\|^2 = \sum_{i=1}^k |g(h_{ip})|^2 = |g(h_{1p})|^2 + |g(h_{2p})|^2 + \dots + |g(h_{kp})|^2 \quad (12)$$

and rearranging the entire channel matrix  $H$  according to the magnitudes of the resulting values as follows:

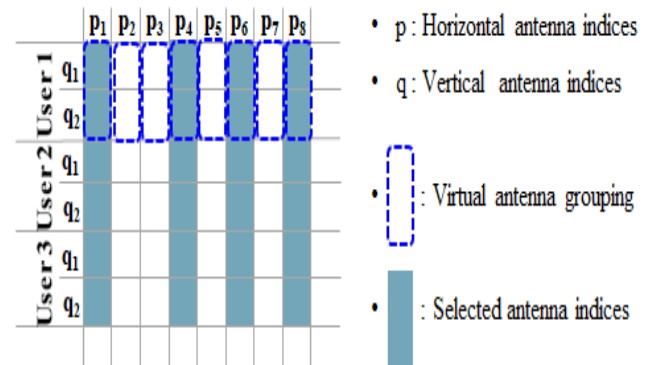

 Figure 3. Channel selection for 2D antenna grouping (e.g., SAI  $\in \{1,4,6,8\}$ ).



TABLE I. SIMULATION PARAMETERS

System parameters	Values	System parameters	Values
Carrier frequency	2.1 GHz	Antenna element spacing	Horizontal: $0.5\lambda$ , Vertical: $0.5\lambda$
Bandwidth	10 MHz	Codebook	KPC by dual DFT codebook
TTI length	10 ms	Scheduler	Max throughput per TTI allocation
Duplexing	FDD	Receiver type	Zero forcing
3GPP scenario	3D-UMa (ISD: 500 m)	HARQ	Maximum of 3 transmissions
Network layout	Hexagonal grid, 1 sector per site	CSI-RS channel estimation	Perfect
Number of UEs per cell	8 (random distribution)	DM-RS channel estimation	Perfect
eNB transmit power	46 dBm	UE Antenna elements	1
eNB height	25 m	UE height	$3*(UE\_floor-1)+1.5$ m
eNB antenna elements	64,32,24,16,12,8	Antenna selection elements	32,24,16,12,8
eNB antenna configuration	(8,8,8), (8,4,8), (4,6,8), (4,4,8), (2,6,8), (2,4,8)	Antenna selection configuration	(8,4,8), (4,6,8), (4,4,8), (2,6,8), (2,4,8)
eNB polarized antenna model	Model-1 from 3GPP TR36.873[7]	Antenna selection scheme	NBS, CBRCS, NRCES <sup>3D</sup>

$$\|g(\tilde{H}_{k1})\|^2 \gg \|g(\tilde{H}_{k2})\|^2 \gg \dots \gg \|g(\tilde{H}_{kp})\|^2 \quad (13)$$

$$\tilde{H}_{NRCES\_3D} = [g(\tilde{H}_{k1}) \ g(\tilde{H}_{k2}) \ \dots \ g(\tilde{H}_{kp})]. \quad (14)$$

The first subset  $S_{NRCES\_3D}^1$  of size  $k \times p$  from  $g(\tilde{H}_{k1})$  to  $g(\tilde{H}_{kp})$  is generated from (14). The subsets are produced by sequentially combining the column vectors of the rearranged matrices in the same way. The subset can be expressed as

$$S_{NRCES\_3D}^j = [g(\tilde{H}_{kj}) \ g(\tilde{H}_{k(j+1)}) \ \dots \ g(\tilde{H}_{k(j+p-1)})]. \quad (15)$$

The subset candidate groups constructed using this method are

$$\gamma_j = Tr\{(S^j S^{jH})^{-1}\}. \quad (16)$$

In (12), if  $(S^j S^{jH})^{-1} = G^j$ ,  $G^j \in C^{K \times K}$ , (11) represents the sum of the diagonal elements of  $G^j$ . The value of (12) can be derived using

$$\gamma_j = \sum_{i=1}^K g_{ii}^j. \quad (17)$$

$S^j$  is calculated based on the maximized signal-to-noise ratio. The subset candidate groups constructed through these methods are

$$j^* = \arg \min\{\gamma_j\}. \quad (18)$$

Therefore, subsets  $S_{NRCES\_3D}^{j^*}$  with  $j^*$  indices are selected as optimal subsets for each subset generation scheme. The 3D-norm-based reduced-complexity exhaustive search (NRCES<sup>3D</sup>) algorithm procedure is summarized in **Algorithm 1**. This algorithm selects the best antenna in the FD-MIMO system.

#### IV. PERFORMANCE ANALYSIS

To verify the performance benefits of antenna selection in FD-MIMO systems, a system-level simulation was performed for a single-cell system environment. The antennas were selected based from a total of 64 antennas and identified using the form  $(n_h, n_v, n_{user})$ . Evaluation was performed for three performance factors: the 3D beamforming gain, according to beam pattern analysis; the SE of the user; and the complexity. The designed 2D antenna group selection was based on the FD-MIMO standard [7] with the following system specifications: 10 MHz transmission bandwidth, 15 kHz subcarrier spacing,

---

**Algorithm 1** Proposed NRCES<sup>3D</sup> algorithm for FD-MIMO systems

---

**Requirement**

1: Best selected antenna indices  $j^*$

**Criterion**

2: Antenna subset selection criterion: maximum SINR

**Repeat**

3: Set the virtual antenna group channel  $H^{3D} \rightarrow g(H^{3D})$  using (7)

4: Rearrange the entire channel matrix  $H$  using (8)–(10)

5: Generate an antenna subset candidate group  $g(S^j)$

6: Select the optimal subset using (12)–(14) until all users

---

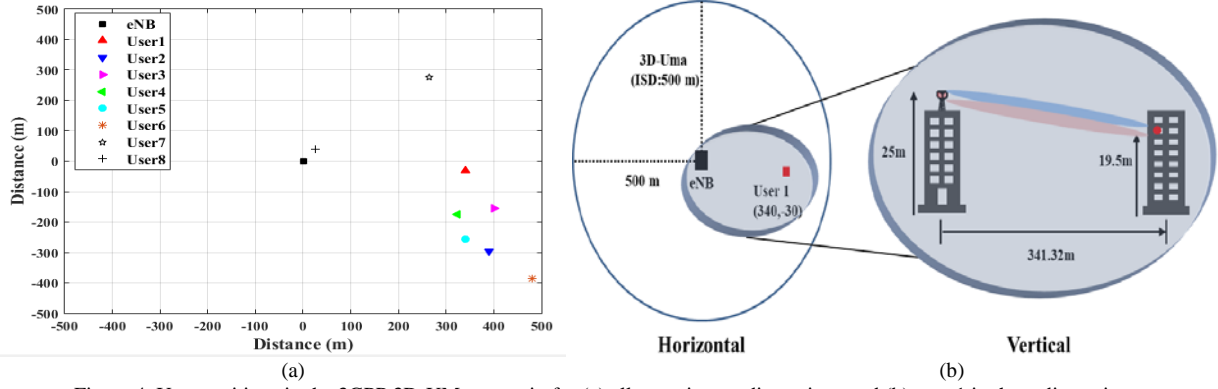


Figure 4. User positions in the 3GPP 3D-UMa scenario for (a) all users in two dimensions and (b) user 1 in three dimensions.

2048 fast Fourier transform size, and 3D-UMa 3GPP scenario. The network layout was one sector per site using a hexagonal grid, and the user equipment (UE) consisted of eight random distributions. The eight users were placed at the following heights in the 3GPP scenario.

The transmitted power was 46 dBm, and the antenna height was 25 m. The system parameters are summarized in Table I. For a 2D antenna array with codebook-based feedback, we used the Kronecker product codebook (KPC) for 3D beam formation. The KPC was designed for azimuth and antenna elevation dimensions and 5 bit code words. Each code word contained angle information about the beam formation through a feedback code word. The code word changed according to the antenna selected, and the beam formation angle changed correspondingly. Fig. 4 shows the location of UE 1 in the 3D-UMa scenario. User 1 was located at (340 m, 30 m), and the antenna height was 19.5 m. Fig. 5 depicts the beam pattern for

the selected antenna of UE 1. The theoretical beam angle for the vertical dimension was  $89.07^\circ$ , and the corresponding feedback code word was 1 ( $86.42^\circ$ ). The antenna selection technique was applied with and without the same. The theoretical beam angle for the horizontal direction was  $95.04^\circ$ , and the corresponding feedback code word was 30 ( $97.18^\circ$ ) and 28 ( $104.48^\circ$ ) when the antenna selection scheme was and was not applied, respectively. The beamforming gain was improved when the antenna selection technique was applied, resulting in improved power performance and overall system efficiency. Among all eight users, three experienced beam gain improvement. As a result of iterative simulation, the beam gain was improved by about 17%.

We next considered the impact of the SE assuming that each of the antennas had the same power. Fig. 6 presents the cumulative distribution functions (CDFs) of the SE results obtained by selecting 32 and eight antennas from a total of 64 antennas. We considered vertical axes with virtual antenna groupings  $q_{\text{num\_group}} = 2$  and  $q_{\text{num\_group}} = 4$ . The simulation was repeated 200 times with one sector fixed. The results reveal that performance improvement was achieved by applying the proposed algorithm. Fig. 7 shows the SE performance resulting from using each algorithm with different numbers of antennas. The values obtained without applying the antenna selection technique are provided for reference, and the SE appears

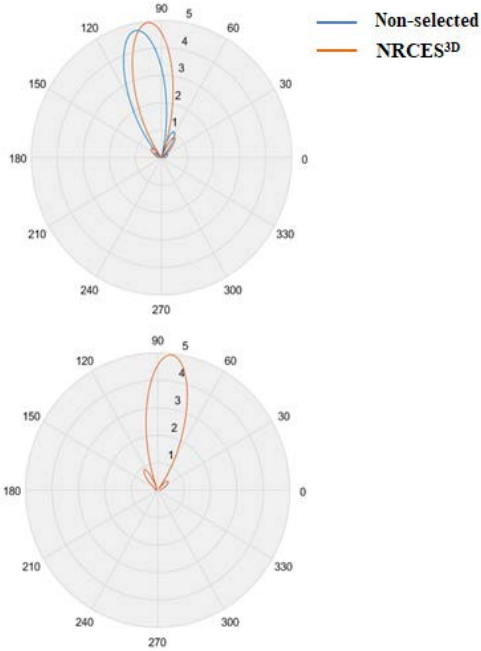


Figure 5. Pattern of 3D beam formation (User 1).

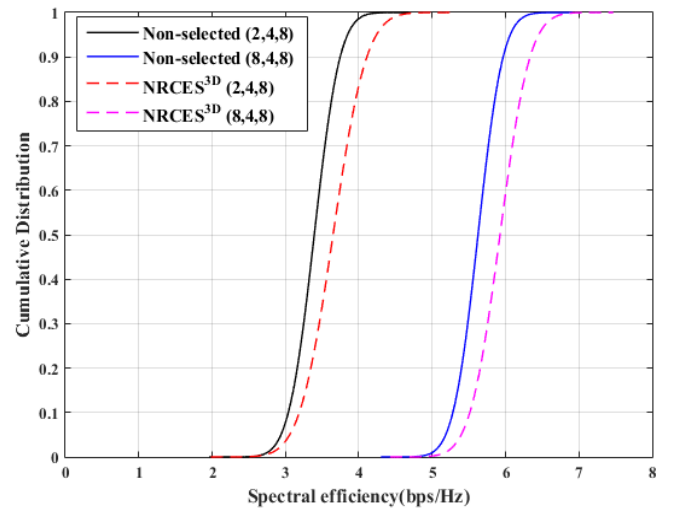


Figure 6. CDF of SE with various antenna configurations.

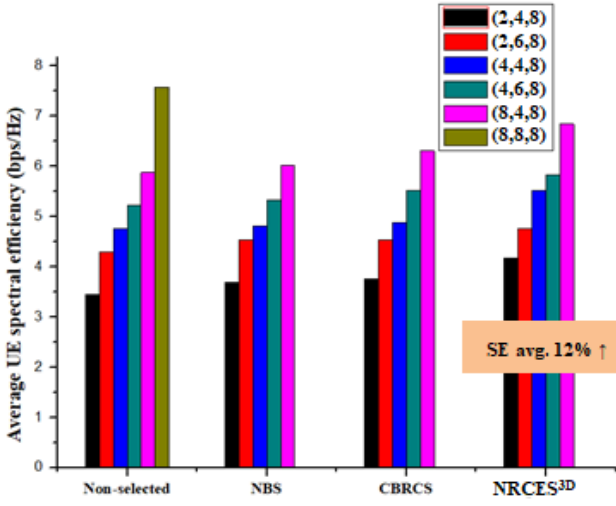


Figure 7. Average SE with various antenna configurations.

improved relative to the reference values by each algorithm. A total of 64 antennas had SAI feedback according to the algorithm, and the average SE of each user was calculated based on the SAI feedback. It was mapped onto the RF chain per SAI, and the number of RF chains was less than or equal to the number of transmitting antennas  $n_t^{RF} \leq n_t$ . Comparison with the non-selection case reveals performance differences upon RF chain reduction. With a constant number of antennas and array, the proposed scheme provided approximately 12% SE improvement.

Finally, we compared the computational complexities of the schemes [8], which are summarized in Table II for FD-MIMO systems with  $N = 64$ ,  $K = 8$ , and  $P = 8$ . The complexity is not related to the vertical axis through antenna grouping. NRCS<sup>3D</sup> exhibits greater complexity than NBS but also provides improved performance.

## V. CONCLUSION

This paper was focused on 2D antenna group selection for FD-MIMO systems, because complexity and RF chain reduction are important issues in 5G mobile communication. We proposed an antenna selection scheme and compared its performance to those of conventional schemes. For this analysis, vertical virtual antenna grouping was performed to enable 3D beam formation. The horizontal antenna group was

selected using three schemes, and the beamforming gain and SE were derived according to the antennas selected. An FD-MIMO system was simulated based on Rel.13. The simulation results demonstrated that the proposed scheme outperforms the previously existing schemes in terms of beamforming gain and SE. In follow-up studies, 2D array antenna selection with FD-MIMO systems will be considered.

## ACKNOWLEDGMENT

This work was supported by Institute for Information & communications Technology Promotion(IITP) grant funded by the Korea government(MSIT). [No. 2016-0-00183, Development of 5G mobile access platform technology based on virtualization converged with computing]

## REFERENCES

- [1] Q. U. A. Nadeem, A. Kammoun, M. Debbah, and M. S. Alouini, "Performance analysis of compact FD-MIMO antenna arrays in a correlated environment," *IEEE Access*, vol. 5, pp. 4163–4178, Mar. 2017.
- [2] O. K. Rayel and G. Brante, J. L. Rebelatto, R. D. Souza, and M. A. Imran, "Energy efficiency-spectral efficiency trade-off of transmit antenna selection," *IEEE Trans. Comm.*, vol. 62, no. 12, pp. 4293–4303, Dec. 2014.
- [3] Y. I. Choi, J. W. Lee, M. J. Rim, C. G. Kang, J. Y. Nam, and Y. J. Ko, "System-level performance of limited feedback schemes for massive MIMO," *ETRI Journal*, vol. 38, no. 2, pp. 280–290, Apr. 2016.
- [4] H. Li, L. Song, and M. Debbah, "Energy Efficiency of Large-Scale Multiple Antenna Systems with Transmit Antenna Selection," *IEEE Trans. Commun.*, vol. 62, no. 2, pp. 638–647, Feb. 2014.
- [5] N. P. Le, F. Safaei, and L. C. Tran, "Antenna selection strategies for MIMO-OFDM wireless systems: An energy efficiency perspective," *IEEE Trans. Veh. Technol.*, vol. 65, no. 4, pp. 2048–2062, Apr. 2016.
- [6] J. Zheng and J. Chen, "Further Complexity Reduction for Antenna Selection in Spatial Modulation Systems," *IEEE Commun. Letters*, vol. 19, no. 6, pp. 937–940, June 2015.
- [7] G. Morozov, A. Davydov, and V. Sergeev, "Enhanced CSI feedback for FD-MIMO with beamformed CSI-RS in LTE-A Pro systems," *Vehicular Technology Conference (VTC-Fall)*, Sept. 2016.
- [8] Y. H. Nam, M. S. Rahman, Y. Li, G. Xu, E. Onggosanusi, J. Zhang, and J. Y. Seol, "Full dimension MIMO for LTE-Advanced and 5G," *Information Theory and Applications Workshop (ITA)*, Feb. 2015.
- [9] 3rd Generation Partnership Project, Technical Specification Group Radio Access Network, "Study on 3D channel model for LTE (Release 12)," *Recommendation 3GPP TR 36.873 V2.1.0*, 2014.
- [10] B. J. Lee, S. L. Ju, N. I. Kim, and K. S. Kim, "The enhanced transmit antenna selection schemes for multiuser massive MIMO systems," *Wirel. Commun. Mob. Com.*, in press. DOI: 10.1155/2017.3463950.

TABLE II. COMPUTATIONAL COMPLEXITY

Algorithm	Operations	Complexity
NBS	$N(2K - 1)$	$1.0 \times 10^3$
CBRCS	$\sum_{i=2}^N i \cdot \left\{ K(N - i + 1)^2 + (N - i + 1) \left( K - \frac{N - i + 1}{2} \right) - \frac{N - i + 1}{2} + 2K^2 + \frac{2}{3} K^3 \right\}$ $+ (N - P + 1) \cdot \left\{ KP^2 + P \left( K - \frac{P}{2} \right) - \frac{P}{2} + 2K^3 + K^2 + K - 1 \right\}$	$1.3 \times 10^7$
NRCS <sup>3D</sup>	$N(2K - 1) + (N - P + 1) \cdot \left\{ KP^2 + P \left( K - \frac{P}{2} \right) - \frac{P}{2} + 2K^3 + K^2 + K - 1 \right\}$	$1.3 \times 10^5$

# Financial analysis of Korean IT service companies and management improvement plan

Focusing on three years after the restriction of participation of large corporations

Hyun-Taek Choi<sup>1</sup>, Seok-Kwan Kim<sup>2</sup>

Department of Computer Science  
Dongshin University  
Naju-si, Republic of Korea  
htchoi@dsic.co.kr, kimseokkwan@dsic.co.kr

Gab-Sang Ryu<sup>3</sup>

Department of Computer Science  
Dongshin University  
Naju-si, Republic of Korea  
gsryu@dsu.ac.kr (corresponding author)

**Abstract**—In this paper, we analyze how the financial structure of medium and small - sized enterprises in IT service companies has changed, before and after restricting the participation of large companies. 148 IT service companies were selected and surveyed. The financial data for the past six years were analyzed by the Korean corporate data crescent and the Financial Supervisory Service (DART), [www.fss.or.kr](http://www.fss.or.kr). As a result of the analysis, large corporations maintain sales and profits through stable internal market, since the restriction of large companies participation, for the past three years, medium and small IT service companies saw sales increase by 23%, but operating profit decreased by 7.3% and net profit decreased by 27.3%. In order for the Software Industry Promotion Act to be successfully established, relevant laws should be revised and complemented.

**Keywords**- *IT Marketing; IT Policy; Management Information; IT Quality Management*

## I. INTRODUCTION

Over 3 years since the enactment of the Software Industry Promotion Act, now. How has the financial structure of a large group of companies that have failed to participate in the public information market and the medium and small sized IT service companies involved changed? After the revision, Kim Mi-ae (KERI policy proposal, 2015) expressed concern in the financial data that the intensification of competition and profitability would be deteriorated due to the financial difficulties of SMEs.[1] In addition, Lee Ho-keun (Korea Economic Research Institute, 2015) analyzed that "the productivity of SMEs participating in public informatization projects will be lower in terms of financials based on the research results." This paper examines the changes in the financial structure of small and medium-sized enterprises (medium and small-sized enterprises for three years (2011, 2012 and 2013) before restricting participation of large corporations and three years (2014, 2015 and 2016) after restricting participation of large corporations). [2][3][4][5][6] In this paper, we examine the business reports published outside the company, such as financial statement (the balance sheet) and the profit and loss statement, for three years before and after the restrictions on participation in large companies were started. Of these, 148 companies were extracted and analyzed. We will analyze the financial status of IT service

companies in Korea in depth and seek ways to improve management in the future. [7][8]

## II. DATA COLLECTION AND ANALYSIS METHODS

### A. Data collection

The research population of this study is "IT services company in 2013 Sales ranking" announced by Korea IT Service Industry Association on July 1, 2014, 113 companies and in March 2014, 148 companies were selected from the 4,596 IT service companies announced by Korea Electronics and Telecommunications Industry Promotion Association. In this paper, the criteria adopted by only 148 IT service companies are as follows. (1) Of the 221 companies with more than 30 billion won in 2013, 19 affiliated companies (exceeding 500 billion won) belonging to the large enterprise group, We also excluded eight companies belonging to a large group of companies exceeding 30 billion won. (2) Among the companies exceeding 30 billion won, game specialists, telecommunication corporations, specialists in the production of electric products, and specialists in hardware products were excluded from participating in the Government it business. (3) Some companies, such as SK, have difficulty in distinguishing only IT service sales because of multiple business areas (non-IT sector), and the non-IT sector influenced other data when adopted. They are excluded from the sample companies. (4) If the company's sales or net loss is large and the six-year financial statements do not have continuity, the data would have a distorted effect on the average of other data. (5) Although the restriction on participation in large corporations took effect in January 2013, the financial data would have been affected in 2014, and the financial data for 2013 was before the restriction on participation in large companies.

### B. Analysis methods

In this paper, rather than verifying financial analysis through statistical analysis of any hypothesis, The financial data of the past six years are extracted from the Korean corporate data CRETOP and the Financial Supervisory Service Electronic Disclosure System (DART, [www.fss.or.kr](http://www.fss.or.kr)). The industry average was calculated all industries by the Bank of



Korea's Economic Statistics System (ecos.bok.or.kr) and J62. (Computer Programming, System Integration and Management) was used as a reference. This data is real and excludes deviations or probabilities used in statistical analysis techniques and is not applied to future predictions.[9][10][11]

### III. RESULTS ANALYSIS

#### A. Growth analysis

It is possible to forecast the competitiveness and profitability of the company in the future as an indicator of how much the size of the company or the performance of the company has increased compared to the previous year.

TABLE I. ANALYSIS BY COMPANY GROWTH POTENTIAL BEFORE AND AFTER RESTRICTING PARTICIPATION OF LARGE COMPANIES

Grade	Indicators	After restricted participation of large corporations 3 years average	After restricted participation of large corporations 3 years average	Amount reduced (after-before)
Large corporation group	Total assets	415,624	486,740	71,117
	Sales amount	511,101	526,438	15,338
Medium and small business	Total assets	49,391	60,754	11,363
	Sales amount	51,288	66,686	11,693

(unit: one million won )

Large companies' participation restrictions In the three years after the restriction, the average sales of large corporations has increased by 3%. On the other hand, medium and small-sized enterprises increased by 23%. Total assets increased by 17% for large companies and 23% for medium and small businesses. The increase in the assets and sales of large corporations caused stable IT investments in the group companies. On the other hand, medium and small enterprises are the result of restricting the participation of large group of companies in the public informatization market due to revision of Software Industry Promotion Act.

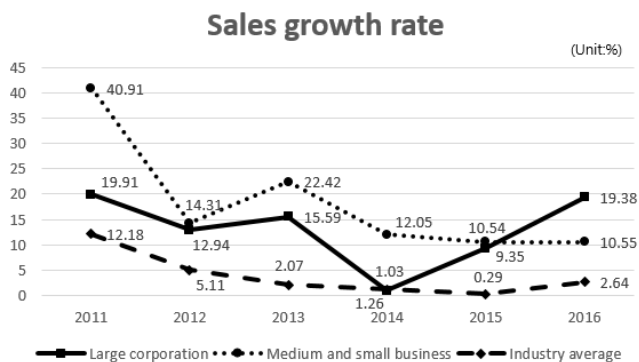


Figure 1. Sales growth rate

The sales growth rate of the large corporations group temporarily decreased to 1.03% in 2014 when the first sales were started due to restrictions on the participation of large companies. However, after 2015, the sales growth rate started to increase again. In particular, the rate of increase is larger than the industry average ratio. Medium- and small-sized companies have steadily maintained their sales growth since the restriction of participation in large companies, but this is because the size of the public information market is the same every year. On the other hand, large corporations have a strong growth potential in the subsidiaries' internal market than the public ones, and the introduction of new technologies is fast.

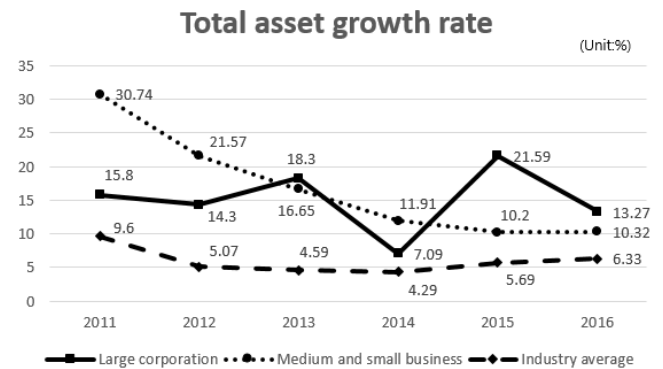


Figure 2. Total asset growth rate

The growth rate of total assets has a pattern similar to the sales growth rate.

#### B. Profitability Analysis

The higher the profitability ratio, the better.

TABLE II. ANALYSIS BY COMPANY PROFITABILITY BEFORE AND AFTER RESTRICTING PARTICIPATION OF LARGE COMPANIES

Grade	Indicators	After restricted participation of large corporations 3 years average	After restricted participation of large corporations 3 years average	Amount reduced (after-before)
Large corporation group	Operating profit	28,868	29,063	196
	Net profit	20,843	21,746	903
Medium and small business	Operating profit	2,879	2,667	-212
	Net profit	2,752	1,998	-753

(unit: one million won )

After the restriction of participation in large companies, large corporations increased their operating profit by 0.67% and net profit by 4.33%. On the other hand, medium and small businesses showed a decrease of 7.36% in operating profit and 27.36% in net profit.

## IV. CONCLUSION

The evaluation of the amendment of Article 24 (2) of the Software Industry Promotion Act should be made after three years of validity of the amendment, so as to analyze whether it meets its purpose. In addition, it is also meaningful to analyze the future direction of the future with only financial data. Large corporations maintained sales and profits through internal affiliate market, although they predicted that restrictions on participation in large companies would have a negative (-) limit on growth potential and profitability. The sales growth rate and the total assets growth rate were lower than before, but the increase in the sales OP margin and the sales net profit ratio was significant. The six-year period in which this paper is based has been negatively influenced by external factors such as financial crisis, reduced IT investment, cloud IT and new IT technologies, and lowered H/W prices for existing systems and decreased IT budget due to political influence. The fact that growth and profit remained stable in spite of the period can be seen as the support of group companies of large corporations expanded. On the other hand, total assets and sales, which represent the growth of medium and small IT service companies for three years after the restriction of participation in large companies, had a positive effect, but operating profits and net profit showed negative effects. In terms of financial statements, revenues increased 23%, but operating profit fell 7.3% and net profit 27.3%. The revision of the Software Industry Promotion Act was revised in terms of policy, but the revision of the Software Industry Promotion Act had a negative impact on the revision of the Software Industry Promotion Act due to the lack of Other laws, such as the National Contract Act and the Subcontract Act. Specifically, (1) it kept the lower amount system of public information business applied to large enterprises, preventing the entry of midsize companies into the public market. (2) Each ministry maintains the system to apply the budget as much as possible but to select a firm with lower price than technology in procurement bidding. (3) The owner often changes the scope of work after the contract from time to time, and even after the inspection, the workforce cannot be withdrawn, but the IT service company must agree. (4) In negotiating technology, we have no choice but to agree on excessive demands. (5) The additional administrative expenses of the companies are increasing due to the relocation of public institution innovation cities, but they are not reflected in the budget. (6) If the maintenance rate is unilaterally lowered and the manufacturer requires the desired rate, if the negotiation fails, the damage to the business will be increased. These causes have led to the failure of profitability for midsize companies focused on public informatization projects. In addition, SMEs are avoiding the growth of medium-sized enterprises, and medium-sized enterprises are in the process of creating separate SMEs. If the law has already been revised but the supervision is not done and It is right for the original purpose of revising the Software Industry Promotion Act to speed up the parts that need to be revised.

## REFERENCES

- [1] Kim Mi-ae, "The Problems of Restrictions on Large Business Participation in the IT Service Industry", KOREA ECONOMIC RESEARCH INSTITUTE, KERI Insight 15-29, Oct 2015.

## Operating profit margin rate

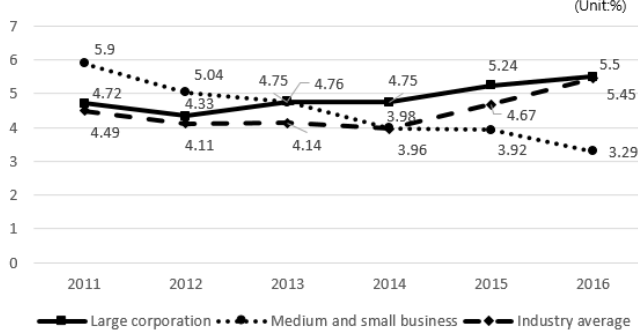


Figure 3. Operating profit margin rate

Sales OP margin Compared to sales, net operating profit(compared to sales), excluding non-operating income, is an indicator of operating efficiency. The large-enterprise group had an average of 4.6% for the three years before restricting large-enterprise participation, and 5.24% for medium and small-sized enterprises. The three-year average after the restriction was 5.16% in the large group, 0.56% in the average, while in the medium and small-sized enterprises it was 3.73%, which was -1.51% worse. Even in the industry average, the industry standard for 2016 is the same for large corporations, but for small and medium-sized companies, it is less than the industry average. Large corporation group has steadily increased from 4.72% in 2011 to 5.5% in 2016, and is similar to the industry average. On the other hand, medium and small-sized enterprises are gradually deteriorating every year since the restrictions on participation of large companies. It is 3.29% in 2016, 2.21% in the large industry group, 4.59% in the peer industry average and 2.16% in the whole industry average.

## Net profit margin rate

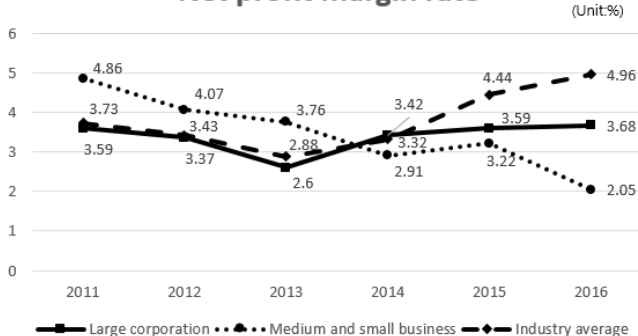


Figure 4. Net profit margin rate

Large companies, such as sales OP margin, are steadily improving regardless of the restrictions on participation by large companies, but small and medium enterprises are continuously falling.

- [2] Lee Jung Keun, "Research for the development of software industry ecosystem", The Korea Society of Management Information System, International Conference, Aug 2015.
- [3] Kim Do Seung, An Young Ha, "The Entry Regulation Against Large Companies in Software Procurement", The Legal Studies Institute of Chosun University, vol. 21, No.1, pp 201-227, 2014
- [4] Kang Cheol Ha, "Law, policy review and development proposal for restrictions on participation in large-enterprise public SW projects", KOREA ECONOMIC RESEARCH INSTITUTE, vol. 2015 no. 11, pp 47-59, 2015
- [5] Sin Ig Ho, Lee Dae Cheol, Sin Eun Hui, Jeon Ji Yeong, Park Du Su, Hwang Seul Gi, "A Study on Impact and Improvement of Major Firm Limitation in Public SW Market", National IT Industry Promotion Agency, Nov 2014.
- [6] Kang Un Sik, "A study on a growth model for IT service companies in Korea", Ph. D. Dissertations, Kookmin University, 2009.
- [7] Yoo Ho Seok, Kang Song Hee, Yoo Jae Hong, "Research on Advancement of Software Ecosystem in Public Sector", Software Policy & Research Institute, Apr. 2016
- [8] Yoo Ho Seok, Kang Song Hee, Kim Jun Yeon, "Institutionalization plan of a Split-Ordering System for Strengthening the Public SW ecosystem", Software Policy & Research Institute, Aug. 2016
- [9] Economic Statistics System, "<https://ecos.bok.or.kr>"
- [10] Data Analysis, Retrieval and Transfer System, "<https://dart.fss.or.kr/>"
- [11] KOREA ENTERPRISE DATA, "<http://www.cretop.com/>"

# Design of 40ns 512kbEEPROM IP

Youngee Kim, Yoongyu Ha, Mincheol Sung, Panbong Ha,

Department of Electronic Engineering, Changwon National University  
Changwon 641-773, Republic of Korea  
Email: pha@changwon.ac.kr

**Abstract** — EEPROM IP for MCU requires 40 ns high speed EEPROM. Therefore, in this paper, current S/A (Sense Amplifier) circuit is used to satisfy 40ns access time. On the other hand, 512kb EEPROM IP uses VPP (= 14.5V) voltage which is HV (High Voltage) used in TEG module for erase and program operation. The layout size of the 512 kb EEPROM IP designed based on the 0.13  $\mu\text{m}$  BCD process is 1676.365  $\mu\text{m}$   $\times$  1508.31  $\mu\text{m}$  (=2.528  $\text{mm}^2$ ).

**Keywords**—EEPROM, IP, VPP, Current S/A, BCD process

## I. INTRODUCTION

Nonvolatile memory IP is used in microcontroller unit (MCU), and nonvolatile memory with high-speed read and write characteristics is required particularly [1][2]. Chip such as wireless charger and USB type-C requires EEPROM IP (Intellectual Property) for MCU that performs real-time information update, security data storage, and command code storage [3-5]. Therefore, a TEG module for EEPROM cell verification using a split-gate EEPROM cell has been introduced [5]. The proposed EEPROM TEG module can measure the  $V_{TE}$  (Erase  $V_T$ ) and  $V_{TP}$  (Program  $V_T$ ) of the EEPROM cell through the DOUT pin using the EEPROM cell  $V_T$  measuring mode. However, since it is a slow part with the access time of 500ns, it can not satisfy that of 40ns required by an MCU.

Therefore, in this paper, current S/A (Sense Amplifier) circuit is used to satisfy 40ns access time [6]. On the other hand, 512kb EEPROM IP issues VPP (= 14.5V) voltage which is HV (High Voltage) used in TEG module for erase and program operation. The layout size of the 512kb EEPROM IP designed based on the 0.13  $\mu\text{m}$  BCD process is 1676.365  $\mu\text{m}$   $\times$  1508.31  $\mu\text{m}$  (=2.528  $\text{mm}^2$ ).

## II. DESIGN OF 512KB EEPROM IP

Table 1 shows the major features of the 512kb EEPROM IP designed using the 0.13  $\mu\text{m}$  BCD process. The EEPROM cell uses a split gate EEPROM cell and has a cell size of 0.97  $\mu\text{m}^2$ . A state in which  $V_T$  is higher than VRD (= 1.5V) by injecting electrons into an FG (Floating Gate) in an EEPROM cell is called a programmed state, and a state in which electrons injected into the FG are ejected and  $V_T$  becomes lower than the VRD voltage is called an erased state [6]. The VDD voltage used is 4.5V to 5.5V and the temperature range is -40°C to 125°C. The operating modes are normal mode, read, page erase, page buffer load, and page program.

TABLE 1. MAJOR SPECIFICATIONS OF 512KB EEPROM IP

Items	Main Features
Process Technology	130nm Process
Memory Density	512Kbit
Cell Array	512R $\times$ 1024C
Supply Voltage (VDD)	4.5V ~ 5.5V
Temperature Range	-40°C ~ 125°C
Normal Mode	Reset/ Power-Down/Stand-by/Read/Page Erase/Program
Write-Verify-Read Mode	Erase-Verify-Read/Program-Verify-Read
Endurance	10K Cycles
Write Time	2ms
Access Time	40ns

The designed 512kb EEPROM IP consist of a cell array of 512rows  $\times$  1024 columns, a BL switch circuit, a BL S/A circuit, a DC-DC converter and a control logic circuit as shown in the block diagram in Fig. 1. This 512kb EEPROM IP uses VPP (= 14.5V) voltage which is HV (High Voltage) used in TEG module for erase and program operation. In the read mode, the SG selected by decoding the row address of A[13:5] is applied with 3.3V while all the CGs are applied with the VRD (= 1.5V) voltage. and thus the EEPROM cells in one of the 512 rows are selected. And the read data of one of the 32 words selected by decoding A[4:0] is transferred to the BL S/A (Sense Amplifier) circuit through the BL switch circuit. The data of the delivered EEPROM cell is output to the DOUT port after sensing [6].

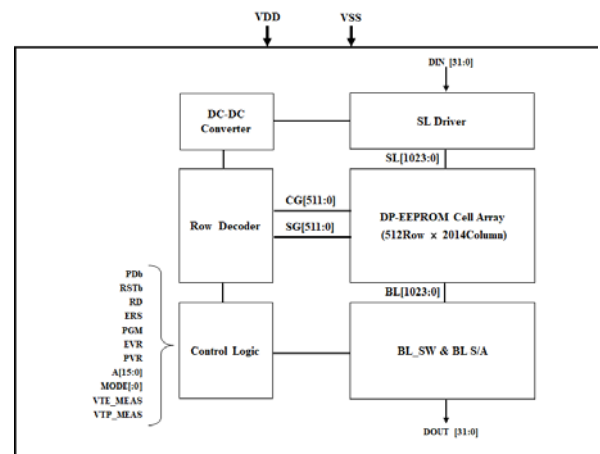


Figure 1. Block diagram of 512Kb EEPROM IP

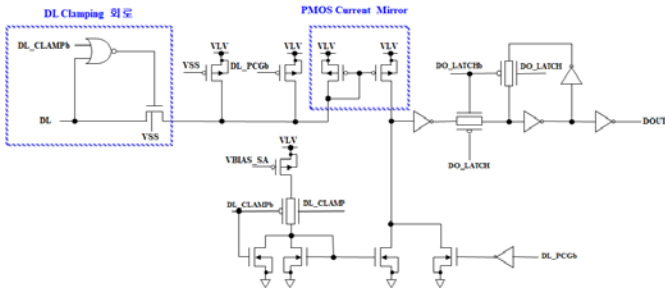
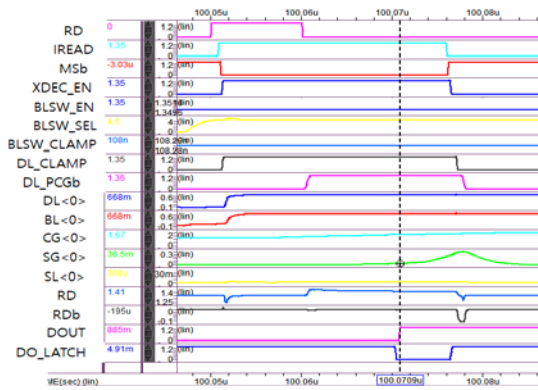
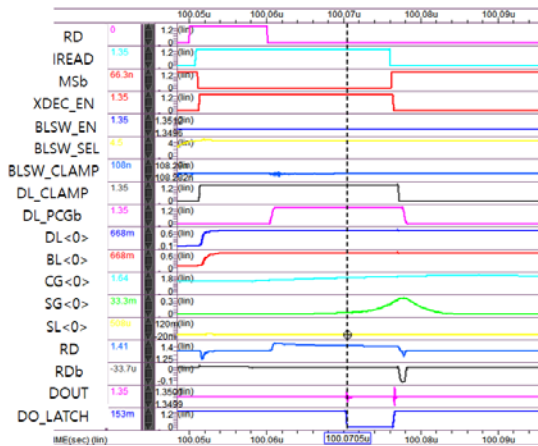


Figure 2. BL S/A circuit[6].

Fig. 3 shows the simulation results of erased cells and programmed cells in read mode. Simulation conditions were  $V_{DD} = 4.5V$ , SS (slow NMOS and slow PMOS) model parameter, Temp. =  $125^{\circ}C$ . As shown in the simulation results, it is confirmed that the access time is 24.2ns, which is less than 40ns.



(a)



(b)

Figure 3. Simulation results in read mode: (a) programmed cell and (b) erased cell.

Fig. 4 shows the layout image of a 512kb EEPROM IP designed based on a  $0.13 \mu m$  BCD process. The IP size is  $1676.365 \mu m \times 1508.31 \mu m (=2.528 mm^2)$ .

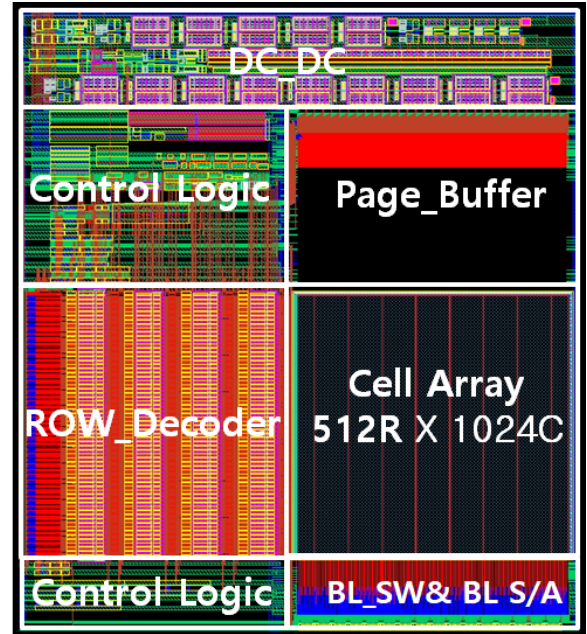


Figure 4. Layout image of 512kb EEPROM IP

### III. CONCLUSION

Wireless charger and USB type-C chips require 40ns EEPROM IP for MCUs that perform real-time information update, secure data storage, and command code storage. Therefore, in this paper, current S/A (Sense Amplifier) circuit is used to satisfy access time of 40ns, and access time of 24.2ns is implemented under slow simulation condition. The layout size of 512kb EEPROM IP designed based on  $0.13 \mu m$  BCD process is  $1676.365 \mu m \times 1508.31 \mu m (=2.528 mm^2)$ .

### REFERENCES

- [1] F. Xu, X. Q. He, L. Zhang, "Key Design Techniques of A 40ns 16K Bits Embedded EEPROM Memory", Communication, Circuits and System, vol. 2, pp. 1516-1520, June 2004.
- [2] A. Conte, G. L. Gudiceo, G. Palumbo, and A. Signorello, "A High-Performance Very Low-Voltage Current Sense Amplifier for Nonvolatile Memory", IEEE J. Solid-State Circuits, vol. 40, no. 2, pp. 507-514, Feb. 2005.
- [3] M. Hatanaka, H. Hidaka, and G. Palumbo, "Value Creation in SOC/MCU Applications by Embedded Non-Volatile Memory Evolutions", Asian Solid State Circuits Conference, pp. 38-42, Nov. 2007.
- [4] Y. H. Kim, H. Park, M. H. Park, P. B. Ha, and Y. H. Kim, "Design of a Fast 256Kb EEPROM for MCU", JKICE, vol. 19, no. 3, pp. 567-574, March 2015.
- [5] Heon Park et al., "Design of a Cell Verification Module for Large-Density EEPROMs," KIICT, vol. 10, no. 2, pp. 176-183, Oct. 2017.
- [6] Younghee Kim et al., "Study on Memory Circuit Structure Analysis," ETRI Report, Oct. 2017.



# Liquid crystal system dispersed with dysprosium oxide ( $Dy_2O_3$ ) nanoparticles

Chan-Woo Oh, Seok-Gon Hwang, Eun-Gon Park, Hong-Gyu Park\*  
 Optoelectronics Laboratory, Department of Electrical, Electronic and Control  
 Changwon National University, Changwon, Republic of Korea  
 E-mail : hgpark@chanwon.ac.kr

**Abstract**— It is well known that liquid crystal (LC) doped with nanoparticles (NPs) can easily change the physical and electro-optical properties of LC mixture. In this study, we reported the doping effects of dysprosium oxide ( $Dy_2O_3$ ) NPs on LC alignment for enhanced LC display (LCD). When the  $Dy_2O_3$  NPs were doped to 1.0 wt.%, it was confirmed that the LC alignment was uniform and stable. The UV transmittance of the LC mixture cell also showed the same tendency as the LC alignment characteristics.

**Keywords:** *dysprosium oxide nanoparticle; liquid crystals; doping concentration; liquid crystal alignment*

## I. INTRODUCTION

Colloidal systems have become an interesting research topic from academia to industry over the past few years. Especially, many researches have been conducted to improve the electro-optical (EO) characteristics of liquid crystal displays (LCDs) using various kinds of nanoparticles (NPs) due to NPs can easily change the physical and EO properties of liquid crystal (LC) mixture. Acharya et al. reported that crystallographic phase induced EO properties of nanorod dispersed LC. [1] Hwang et al. have shown that a good LC orientation can be achieved without an alignment layer and the pretilt angle of LCs can be controlled in polyhedral oligomeric silsesquioxanes (POSS)-doped LCD. [2] In addition, other groups reported improved performance characteristics such as faster response times and lower threshold voltages because of high dielectric anisotropy or reduced screening effect through NPs doped LC cells. [3,4]

For this study, as a suitable material for changing the physical and EO properties of the LCs, a lanthanum oxide is assumed such as  $Dy_2O_3$ , [5]  $Ho_2O_3$ ,  $Gd_2O_3$ ,  $Pr_2O_3$  and  $La_2O_3$ . Among these materials,  $Dy_2O_3$  oxides are widely used in various fields such as optoelectronics and memory devices due to high dielectric constants, large band gaps and high thermal stability. For these reasons, it is possible to change the physical properties of LC mixture by doping lanthanide oxide NPs in LCs and cause the EO characteristics to be improved. [6] In this study, we reported the doping effects of  $Dy_2O_3$  NPs on LC alignment.

## II. EXPERIMENT

Before preparing the LC alignment layer, an ITO-coated glass (Samsung Corning 1737) was cleaned with a supersonic

wave in a bath using acetone, isopropyl alcohol, and a deionized water solution for 10 min and finally dried with  $N_2$  gas. A 50-nm thick homeotropic polyimide (PI) layers were coated onto glass substrates using a spin coater. These substrates were prebaked at 80 °C for 10 min on a hot plate. After then in the oven substrates were hard baked at 180 °C for 1 h.  $Dy_2O_3$  NPs were purchased from Sigma Aldrich Korea Co. The mixture of  $Dy_2O_3$ /LC (VA-J70, LIXON) was prepared at difference concentrations (0.5, 1.0, 1.5 and 2.0 wt.%). Prepared the  $Dy_2O_3$  NPs/LC mixtures were injected into the empty cells via capillary force at room temperature. The substrates were fabricated with a cell gap of 60  $\mu m$  to observe LC alignment state and UV-VIS transmittance of LC mixture cells. X-ray diffractometer (XRD) analysis was performed using a X'Pert PRO MPD (Philips) to identify the crystallinity of the  $Dy_2O_3$  NPs. The alignment states of the  $Dy_2O_3$  NPs/LC mixtures were observed by a photomicroscope (BXP 51, Olympus). The UV-Vis transmittances of the LC cells with pristine and  $Dy_2O_3$  NPs doped LC was measured by UV visible near infra-red (UV-VIS-NIR) spectrometer measurements (V-670, JASCO).

## III. RESULTS AND DISCUSSION

We have characterized the  $Dy_2O_3$  NPs by taking its XRD pattern which is shown in Fig. 1. The strong peaks at  $2\theta = 20.3^\circ, 28.9^\circ, 33.5^\circ, 43.2^\circ, 48.2^\circ$  and  $57.2^\circ$  correspond to the reflections of the (211), (222), (400), (440), (622) and (662) planes, respectively. The  $Dy_2O_3$  NPs appeared to have cubic structures, based on comparison with the standard pattern JCPDS card No. 86-1327. The typical size of  $Dy_2O_3$  NPs is around 30 nm which is calculated using Debye-Scherrer formula.

The alignment characteristics of the LC mixture cells doped with different concentrations of  $Dy_2O_3$  NPs were observed. Figure 2 shows the LC alignment states of LC mixture cells doped with none, 0.5 wt.%, 1.0 wt.%, 1.5 wt.% and 2.0 wt.% NPs concentrations. As shown in Fig 2, the LC mixture cells with 0.5wt.% and 1.0wt.%  $Dy_2O_3$  NPs concentrations show tiny aggregations compared with the pristine LC cell. However, these aggregations were too small to be seen at all in actual naked eye. In case of LC cell with 1.5 wt.% and 2.0 wt.%  $Dy_2O_3$  NPs concentration, more and larger NPs aggregations were observed. These results indicate that the  $Dy_2O_3$  NPs doping concentration should not exceed 1.5 wt.%.

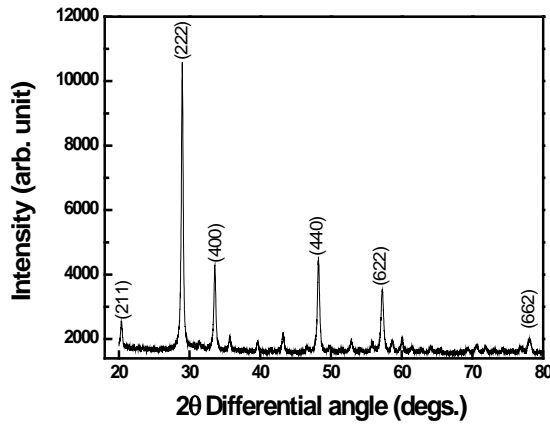
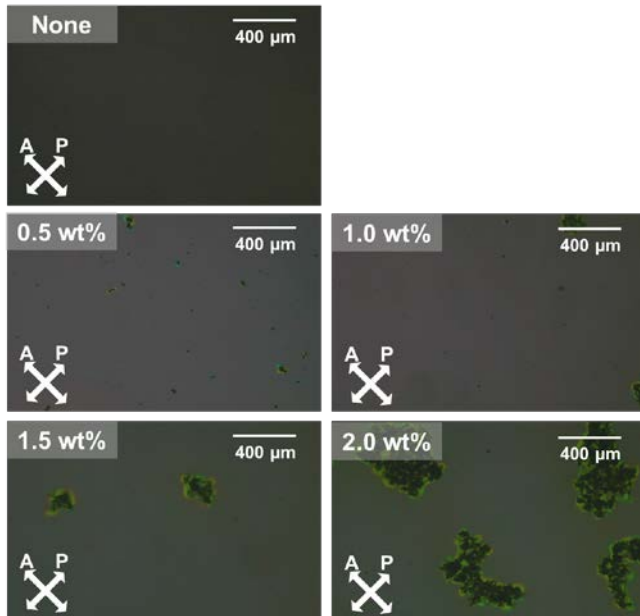
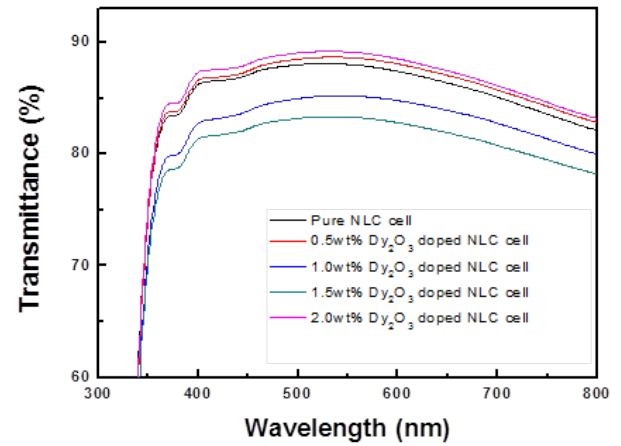
Fig 1. XRD pattern of  $\text{Dy}_2\text{O}_3$  NPs.Fig 2. Photomicrographs of LC cells doped with a pristine, 0.5 wt.%, 1.0 wt.%, 1.5 wt.% and 2.0 wt.%  $\text{Dy}_2\text{O}_3$  NPs concentration. (A: Analyzer, P: Polarizer)

Figure 3 shows the transmittance spectra of LC mixture cells doped with various concentrations of  $\text{Dy}_2\text{O}_3$  NPs. A pure LC cell was used for comparison. Over the wavelength range of 420–780 nm, the average optical transmittances of the pure and the  $\text{Dy}_2\text{O}_3$  NPs dispersed LC mixture cell were 86.38%, 86.95%, 83.62%, 81.80%, 87.44%, respectively. As can be seen, the transmittance of LC mixture cells became degraded as a function of doping concentration except for the 2.0 wt% LC mixture cell. The degradation of transparency occurred due to NP agglomeration, which caused light scattering. At a  $\text{Dy}_2\text{O}_3$  concentration of 2.0 wt%, the transmittance is increased because the NP aggregation is shifted to one side and the transmittance is partially increased.

Fig 3. UV-VIS transmittance spectra of LC mixture cells doped with 0.5 wt.%, 1.0 wt.%, 1.5 wt.% and 2.0 wt.%  $\text{Dy}_2\text{O}_3$  NPs at room temperature, respectively, and a pristine LC cell that was used as a reference.

#### IV. CONCLUSIONS

In conclusion, we investigated the alignment states of  $\text{Dy}_2\text{O}_3$  NPs doped LC mixture cells. The photomicrographs of  $\text{Dy}_2\text{O}_3$ /LC mixture showed uniform and stable LC alignment. The particle-induced aggregations were observed in the LC mixture cells but these did not affect LCD quality up to 1.0 wt.% concentration. Consequently, we achieved uniform LC alignment state by doping  $\text{Dy}_2\text{O}_3$  NPs and this approach could lead to enhanced EO characteristics of LCD.

#### References

- [1] S. Acharya, S. Kundu, J. P. Hill, G. J. Richards, and K. Ariga, "Nanorod-driven orientational control of liquid crystal for polarization-tailored electro-optic devices," *Adv. Mater.* vol. 21, pp. 989-993, January 2009.
- [2] S.-J. Hwang, S.-C. Jeng, and I.-M. Hsieh, "Nanoparticle-doped polyimide for controlling the pretilt angle of liquid crystals devices," *Opt. Express* vol. 18, pp. 16507-16512, August 2010.
- [3] Y.-S. Ha, H.-J. Kim, H.-G. Park, and D.-S. Seo, "Enhancement of electro-optic properties in liquid crystal devices via titanium nanoparticle doping," *Opt. Express* vol. 20, pp. 6448-6455, March 2012.
- [4] H.-Y. Jung, H.-J. Kim, S. Yang, Y.-G. Kang, B.-Y. Oh, H.-G. Park and D.-S. Seo, "Enhanced electro-optical properties of  $\text{Y}_2\text{O}_3$  (yttrium trioxide) nanoparticle-doped twisted nematic liquid crystal devices," *Liq. Cryst.*, vol. 39, pp. 789-793, April 2012.
- [5] D.-W. Kang, T.-G. Park, J.-W. Kim, J.-S. Kim, H.-S. Lee, and H. Cho, "Effect of dysprosium oxide addition on the microstructure and dielectric properties of  $\text{BaTiO}_3$  ceramics," *Electron. Mater. Lett.*, vol. 6, pp. 145-149, December 2010.
- [6] W.-S. Koo, H.-K. Chung, H.-G. Park, J.-J. Han, H.-C. Jeong, M.-J. Cho, D.-H. Kim, and D.-S. Seo, "Enhanced switching behavior of iron oxide nanoparticle-doped liquid-crystal display," *J. Nanosci. Nanotechnol.* vol. 14, pp. 8609-8614, November 2014.